國 立 交 通 大 學

光 電 工 程 研 究 所

碩 士 論 文

氮化銦之兆赫輻射與二次諧波及其載子動力學

THz Radiation, Second Harmonic Generation, and Carrier Dynamics from InN surface

研 究 生：余科京

指導教授：安惠榮 教授

中 華 民 國 九 十 八 年 七 月

氮化銦之兆赫波與二次諧波及其載子動力學

THz Radiation, Second Harmonic Generation, and Carrier Dynamics from InN surface

研 究 生：余科京　　Student：Ke-Jing Yu

指導教授：安惠榮 教授　　Advisor：Prof. Hyeyoung Ahn

國立交通大學

光電工程研究所

碩士論文

A Thesis
Submitted to Department of Photonics and
Institute of Electro-Optical Engineering
College of Electrical Engineering
National Chiao Tung University
In partial Fulfillment of the Requirements
for the Degree of
Master of Science
in

Electro-Optical Engineering

July 2009
Hsinchu, Taiwan, Republic of China

中 華 民 國 九 十 八 年 七 月

氮化銦之兆赫輻射與二次諧波及其載子動力學之研究

學生：余科京　　　　　　　　　　　　　　指導教授：安惠榮教授

國立交通大學光電工程研究所

摘　要

我們利用兆赫波輻射光譜研究氮化銦的輻射機制，其包含瞬時光電流效應和光整流效應。我們計算出 wurtzite 結構晶體的二階非線性光學之塊體和表面電場感應的電偶響應，進而透過計算結果，兆赫波的入射角、方向角、極化角度相關趨勢得到良好的擬合結果。在低功率激發下，氮化銦的輻射機制主要由瞬時光電流所領導; 隨著激發強度提高，非線性趨勢更加明顯。經由比對兆赫波的方向角、極化角之趨勢，我們推測出瞬時光電流和光整流對於氮化銦的兆赫輻射影響。

二次諧波與光整流同屬於二階非線性光學響應，我們利用先前計算結果成功驗證非對稱晶體的二次諧波主要由塊體電偶響應支配其他表面的響應。實驗上所得到的擬合係數與理論計算相符。

利用時間解析的光激發探測技術，我們研究氮化銦薄膜和其奈米柱的瞬時載子特性，並發現在奈米柱中的載子有較短的生命期，推測是因奈米柱的結構會產生較多的缺陷而使得載子有較快的捕捉時間。我們觀察到薄膜的生命期與載子濃度之間的反比趨勢，但因由缺陷濃度會影響載子的生命期，各樣品的缺陷濃度不一致使此反比趨勢些微誤差。

THz Radiation, Second Harmonic Generation, and Carrier Dynamics from InN surface

Student：Ke-Jing Yu Advisors：Prof. Hyeyoung Ahn

Department of Photonics and Institute of Electro-Optic Engineering, College of Electrical Engineering
National Chiao Tung University

Abstract

THz emission mechanisms for InN are investigated by using THz emission spectroscopy (TES). The second-order optical response of bulk and surface electric field for wurtzite crystal could successfully explain the incident angle-, azimuthal angle-, and pump polarization- dependence of emitted THz field. According to the azimuthal angle- and pump polarization- dependence of TES, we deduced the interplay of transient current and optical rectification in THz emission for InN.

Second harmonic generation (SHG) is the second-order optical response similar to optical rectification. From the calculated results we successfully demonstrated that bulk electric-dipole contribution dominates any surface contribution in SHF for noncentrosymmetric crystal. The best fitting parameters to azimuthal angle dependent SHG experiment are consistent with the calculated results based on bulk electric-dipole contribution.

We also investigated the transient carrier dynamics for InN epilayer and nanorods via time-resolved optical pump-probe technique. The time evolution of transient reflectivity changes of InN is the interplay of photoinduced absorption and band-filling. The pump fluence independent lifetime of InN epilayer is regarded as defect-related recombination time. We also observe an inverse relationship between carrier lifetime and carrier concentration.

Acknowledgement

在碩士班兩年，雖然研究過程辛苦但也使我成長許多，體驗到研究的迷人之處，學習到正確的態度，感謝我的指導教授安惠榮老師無私的教導，指引我研究方向及指導正確的研究觀念。感謝王怡超學長在實驗系統架設的幫忙及雷射的維護，陳晉偉學長在二次諧波方面的指導。平時與洪誌彰學長的研究討論讓我收穫很多，學長廣泛地學習以及做事的高效率值得學習，還要感謝潘悉靈老師實驗室的同學陪伴我兩年的修課及實驗，呂助增老師實驗室親切地交流分享二次諧波的研究，還有實驗室的伙伴陪我度過最重要的碩二。最後，要感謝家人的支持及協助讓我能無後顧之憂地完成碩士研究。

Contents

Abstract(C)………………………………………………………………. i

Abstract(E) ……………………………………………………………… ii

Acknowledgement…………….. iii

Contents……………………………………………………………….. iv

1 Introduction

1-1 Motivation…………………………………………….................. 1

1-2 Organization of this Thesis…………………………..................... 3

Reference…………………………………………………….…………. 4

2 Indium Ntride

2-1 The material properties of InN in optical and THz spectral range 5

2-2 The optoelectronic applications for II-N semiconductors in nonpolar orientation ………………………………………..…... 7

References……………………………………………...…….. 9

3 THz emission and Second-harmonic-generation from a-plane InN

3-1 THz emission mechanism…………………………….……... 10

3-1.1 Transient Current……………………………….…………… 10

Drift Current via Surface Depletion Field……………………. 12

Diffusion Current via Photo-Dember Effect………………… 13

3-1.2 Instantaneous Nonlinear Polarization
(Optical Rectification)…………………………………….. 15
Bulk Seocnd-Order Optical Response………………………. 16

Surface Second-Order Optical Response……………………. 22

3-2 Experimental Setups.. 33

3-2.1 THz emission Measurement system................................. 33

3-2.2 Reflection Second Harmonic Generation (RSHG) Setups.. 36

3-3 Results and Discussions…………………………………………... 37

3-3.1 Reflection SH Generation from InN…………………….. 37

3-3.2 Azimuthal Angle Dependence of THz Emission from InN 43

3-3.3 Pump Polarization Dependence of THz Emission from
InN…………………………………………………………... 49
3-3.4 The comparison between SH generation and THz
emission from InN……………………………………... 53
References……………………………………………………… 55

4 Carrier Dynamics of InN

4-1 Background…………………………………………………... 58

4-1.1 Transient Photo-Reflection………………………………. 58

4-1.2 Scattering Processes in Ultrafast Regime…………..…….. 60

4-1.3 Effects of Carrier Generation…………………………... 63

4-1.3.1 Band-Filling Effect……………………………… 63

4-1.3.2 Band-Gap Renormalization 64

4-2 Experimental Setups…………………………………………………… 66

4-3 Results and Discussions…………………………………………….. 67

4-3.1 Fluence Dependent Carrier Dynamic in InN film and nanorod……………………………………………………… 67

4-3.2 Concentration Dependent Carrier Lifetime 72

References…………………………………………………………. 73

5 Conclusions and Future Work

5.1 Conclusions……………………………………………………….. 75

5.2 Future Work……………………………………………………….. 75

Chap 1. Introduction

1-1. Motivation

Terahertz (THz) radiation lies in the frequency gap between the infrared and microwaves, typically is referred to as the frequencies from 100 GHz to 10 THz. 1 THz is equivalent to 33.33 cm^{-1}(wave numbers), 4.1 meV in photon energy, or 300 μm in wavelength. Two main directions of THz development are THz imaging in bio- and medical fields and THz spectroscopy which has long been inaccessible due to the difficulty in generation of strong, coherent THz waves. Despite several pioneering breakthroughs, searching for the methods to generate reliable coherent THz radiation is still a critical issue in THz science community. One of the simple and efficient methods is to excite the semiconductor surface with sub-picosecond laser pulses. Up to now, *p*-type InAs is known to be the strongest THz emitter under no bias. Recently, due to the small intrinsic bandgap (0.7 eV) and quite large gap (2.8 eV) of the next valley, InN has been inspired potential application in THz region such as efficient THz emitter/receiver. The main THz emission mechanism of InN is photo-Dember effect like InAs; however, THz radiation magnitude from InN films is typically one order less than that from InAs [1-1, 1-2]. Recently, Ahn *et al*. has reported THz emission enhancement from vertically aligned InN nanorod arrays [1-3] and nonpolar orientation (*a*-plane) InN film [1-4], which is at least ten times stronger in amplitude than that from polar (*c*-plane) InN film. To investigate the limitation of THz emission from InN, fully understanding of the emission mechanism involving transient current and instantaneous nonlinear polarization is quite important. In general, the main THz emission mechanism of *c*- and *a*-plane InN is regarded as photo-Dember effect [1-3] at low excitation. In addition to transient current, the influence of optical rectification (OR) from *a*-plane InN becomes significant at high excitation density [1-4]. We conducted the azimuthal angle and pump polarization dependence of THz radiation

measurement from InN to reveal the important information of optical rectification contribution. In addition, we also investigated bulk and surface-electric-field (SEF) induced second-order optical response of wurtzite crystal. The calculated results based on the second-order optical response successfully duplicated experimentally observed angular dependence. The interplay of transient current and optical rectification is also investigated in this work.

Second harmonic generation (SHG) is considered as second-order optical response similar to optical rectification. SHG has been identified as a tool for studying bulk and surface symmetry in materials. Since InN is not centrosymmetric, one can expect that bulk dipole contribution dominates any surface term. Reflection SHG from InN film has significant six-fold rotation symmetry about surface normal which is well described by our calculation of bulk electric dipole contribution.

Many direct bandgap semiconductors generate THz radiation when they are optically excited by femtosecond pulses; however, their performance as THz emitters varies dramatically. In general, THz emission strength depends on the electron and hole mobility. In the quasi-classical approach to electron transport in semiconductors, the mobility parameter is used to describe the scattering events taking place in the material. Through the time evolution of carrier dynamics and THz emission, we found that carrier scattering and non-radiative recombination would occur when THz emission takes place. It means that these mechanisms may influence THz radiation. The pump fluence dependence of carrier dynamic of InN film and nanorods was studied by optical pump-probe spectroscopy. Additionally, concentration dependent lifetime of InN film is observed.

1-2. Organization of this Thesis

In this work we calculated bulk and surface-electric-field induced second-order optical polarization for wurtzite structure crystal. Basing on the calculation results, we explored the azimuthal angle and pump polarization dependence of THz radiation from *c*- and *a*-plane InN film surface. The azimuthal angle dependence of reflection SHG from both *c*- and *a*-InN was examined and well described by our calculations. Besides, we investigated the carrier dynamic of InN film and nanorods.

In chapter 1, our motivation in this work is briefly introduced. In chapter 2, we introduce the material properties including growth condition and optical properties of InN in optical and THz range. In chapter 3, we studied reflection SHG and THz radiation. We present the analysis theories and origins of the second-order optical responses of wurtzite crystal. Then, experimental arrangements are presented, which contain ultrafast laser source, electro-optic sampling based THz emission spectroscopy (TES-EOS), and reflection SHG system. Finally, we present and discuss the azimuthal and polarization rotation angle-dependent results. In chapter 4, we focus on carrier dynamics in InN film and nanorods. In the beginning, we introduce scattering process and effect of carrier generation which are relevant to the investigation in this chapter. After that, an optical pump-probe spectroscopy used in exploring ultrafast dynamic is described. Eventually, we discuss pump fluence dependent carrier dynamics and concentration dependent carrier lifetime. Finally, our conclusion and future work are shown in chapter 5.

1896

References

[1-1] R. Ascazubi ,I. Wilke, K. Denniston, H. Lu, and W. J. Schaff, “Terahertz emission by InN,” Appl. Phys. Lett. **84** 4810 (2004)

[1-2] G.. D. Chern, E D. Readinger, H. Shen, M. Wraback, C. S. Gallinat, G. Koblmuller, and J. S. Speck, “Excitation wavelength dependence of terahertz emission from InN and InAs,” Appl. Phys. Lett. **89** 141115 (2006)

[1-3] H. Ahn, Y. P. Ku, Y. C. Wang, C. H. Chuang, S. Gwo, and C. L. Pan, “Terahertz emission from vertically aligned InN nanorod arrays,” Appl. Phys. Lett. **91** 132108 (2007)

[1-4] H. Ahn, Y. P. Ku, C. H. Chuang, C. L. Pan , H. W. Lin, Y. L. Hong, and S. Gwo, “Intense terahertz emission from a-plane InN surface,” Appl. Phys. Lett. **92** 102103 (2008)

Chap 2. Indium Nitride

2-1. The material properties of InN in optical and THz spectral range

In this work, the *a*-plane InN epitaxial film (~1.2 μm) was grown by plasma-assisted molecular beam epitaxy (PA-MBE) on *γ*-plane $\{1\bar{1}02\}$ sapphire wafer, while the *c*-plane $(000\bar{1})$ InN epitaxial film (~2.5 μm) was grown on Si(111) using a double-buffer layer technique. The back side of *γ*-plane sapphire wafer was coated with a Ti layer for efficient and uniform heating during the PA-MBE growth. The growth direction of the InN film was determined using a 2θ-ω x- ray diffraction scan. Near-infrared photoluminescence was detected from the as-grown *a*- and *c*-plane InN films at room temperature. Unintentionally doped *n*-type carrier concentrations of 7.0×10^{18} and 3.1×10^{18} cm^{-3} and electron mobilities (μ) of 298 and 1036 cm^2/Vs were determined by room-temperature Hall effect measurements for *a*- and *c*-plane InN film, respectively. InN has wurtzite structure with bulk symmetry, 6mm as shown in Fig. 2-1. The atom arrangement in the surface of *a*- and *c*-plane InN is plotted in Fig. 2-2.

The dispersion of optical properties is one of the most important material properties. The optical constants of the InN layers has been determined by spectroscopic Ellipsometry operating at the spectral range between 0.6 and 4.2 eV [2-1] and by terahertz-time domain spectroscopy (THz-TDS) operating at THz range [2-2]. Recently, the frequency-dependent terahertz conductivity of InN epilayer has been investigated by THz-TDS [2-2] and reveals Drude-like behavior.

The InN nanorods (750 nm) were grown on Si_3N_4/Si(111) at sample temperature of 330°C (LT-NR). The N/In flux ratios was ~2.6 for LT-NR and was adjusted at different growth temperature to ensure that the growth proceeded in the columnar mode. The morphologies and size distribution of InN nanorods were analyzed using field-emission scanning electron microscopy. The SEM image of the

hexagonal- shaped LT-NR exhibits nanorods with a uniform diameter of ~130 nm. The LT-NR exhibits an average aspect ratio (height/diameter) of ~6 and an aerial density of ~5×10^{9} cm^{-2}. The frequency dependent refractive index and conductivity are determined by THz-TDS [2-2] at THz frequency range. The frequency dependence is well-described by Drude-Smith model which modify the backward scattering events of carriers.

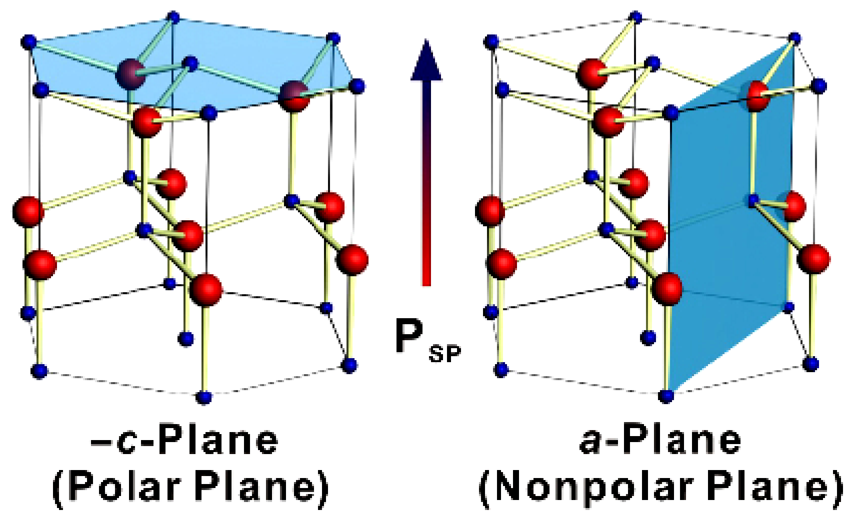

Figure 4-3. The diagram of wurtzite structure of InN.

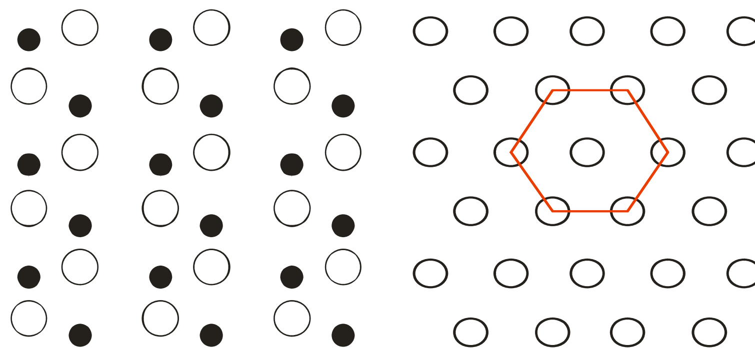

Figure 4-2. The atom arrangement of *a*- and *c*-plane surface of InN.

2-2. The optoelectronic applications for III-N semiconductors in nonpolar orientation

III-Nitride group semiconductors have a wurtzite structure which posses a strong built-in polarization field including spontaneous polarization and piezoelectric polarization results from (In^+, Ga^+, Al^+…)-N^- arrangement. From the lattice orientation, it is divided into polar plane (*c*-plane) and nonpolar plane (*a*- and *m*-plane). These inhomogeneous properties of lattice influence the distribution of photo-current and electric field and even the optoelectronic properties. Hence, the effect of polarization field has been investigated and is an important issue in application for III-N group semiconductor. We discuss the consequences of the very large electrostatic fields that exist within thin layers. The positive and negative charges in material would be separated along the direction of polarization field, and they accumulated at the two sides of polarization field or at the discontinuous region of the field. The carrier accumulation due to polarization field results in the band bending and varies the band-gap and the relative potential of electrons and holes. The carrier accumulation directly affects the radiative recombination rate and leads to redshift in emission. P. Waltereit *et al* [2-3] has proposed a way to remove the electrostatic field via nonpolar growth. In the nonpolar orientation, the material will not carry spontaneous polarization components. The band profile of material grown in nonpolar direction would thus be unaffected by electrostatic fields. It means that the nonpolar material exhibits higher transition energy and electron-hole overlap of essentially unity. P. Waltereit *et al* represented fast radiative recombination time and blueshift in luminance emission for nonpolar plane (*m*-plane) multiple quantum wells. At the room temperature, this fast radiative lifetime for nonpolar samples results in high quantum efficiency.

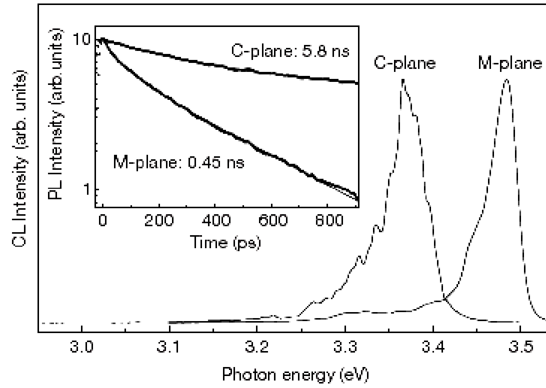

Figure 2-3. The effect of electrostatic field on emission properties of GaN/(Al,Ga)N multiple quantum wells. The blueshift in emission and fast radiative lifetime of *c*-plane with respect to the electric-field-free *m*-plane are the consequences of the intrinsic polarization field. [2-3]

In addition, terahertz emission efficiency has been improved by using the nonpolar crystal orientation. The dramatic terahertz emission enhancement of *a*-plane InN [see Fig. 2-4] has been observed by Ahn *et al* [2-4]. In the nonpolar orientation, the intrinsic polarization field parallel to surface can induce a photo-current along the sample surface. It is well-known that the radiation of in-plane current is more efficient than that of current normal to surface due to the limited surface emission cone. Therefore, photo-carrier induced terahertz radiation can be enhanced via nonpolar growth.

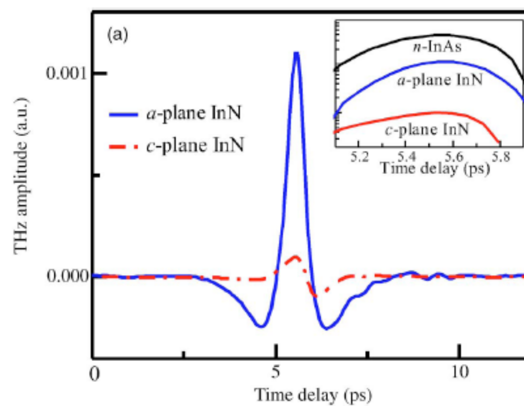

Figure 2-4. THz emission amplitude from *a*- and *c*-plane InN film. [2-4] Inset shows the comparison between *n*-type InAs and *a*-plane InN.

Reference

[2-1] H. Ahn, C. H. Shen, C. L. Wu, and S. Gwo, “Spectroscopic Ellipsometry study of Wurtzite InN Epitaxial Films on Si(111) with Varied Carrier Concentrations,” Appl. Phys. Lett. **86** 201905 (2005)

[2-2] H. Ahn, Y. P. Ku, Y. C. Wang, C. H. Chuang, S. Gwo, and C. L. Pan, “Terahertz spectroscopic study of vertically aligned InN nanorods,” Appl. Phys. Lett. **91** 163105 (2007)

[2-3] P. Waltereit, O. Brandt, A. Trampert, H.T. Grahn, J. Menniger, M. Ramsteiner, M. Reiche, and K. H. Ploog, “Nitride semiconductors free of electrostatic fields for efficient white light-emitting diodes,” nature **406** 865 (2000)

[2-4] H. Ahn, Y. P. Ku, Y. C. Wang, C. H. Chuang, S. Gwo, and C. L. Pan, “Terahertz emission from vertically aligned InN nanorod arrays,” Appl. Phys. Lett. **91** 132108 (2007)

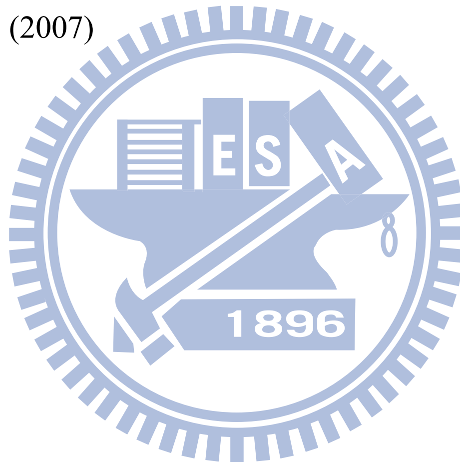

Chap 3. THz emission and Second-harmonic-generation from a-plane InN

3-1. THz emission mechanism

The emission of THz radiation from semiconductor surfaces is very complicate due to multiple competing mechanisms leading to the radiation. Contributions from photo-carrier acceleration in the depletion field, photocarrier diffusion, and optical rectification have all been reported [3-1, 3-2, 3-3]. The relative magnitude of radiation resulting from the various processes is strongly dependent on excitation fluence. To investigate the limitation of THz generation, full recognizing of all different mechanisms leading to emission is quite important.

3-1-1. Transient Current

By means of above band-gap (resonant) nature of the excitation process, in a conventional transport picture one assumes that electron-hole pairs (EHP) are created by vertical transitions in real space within the penetration depth of the incident optical field. Subsequently, EHPs are accelerated by the surface depletion/accumulation field and diffuse to semiconductor inner due to gradient concentration, which leads to drift current and diffusion current, respectively. The photo-generated free carriers are expected to flow in surface normal direction and can be the source of THz wave in Maxwell equation. The direction of transient current leads to azimuthal angle independent optical property of THz field. Under steady pump power fluence, the pump polarization issue can be neglected if we ignore Fresnel coefficient for T_p and T_s. The transient current induced THz field is proportional to photoexcited carrier density n and the mobility μ for electron and hole.

To study the photoexcited THz radiation from semiconductors, we qualitatively describe the electric field **E** in dipole approximation when the carrier's velocity is much less than the velocity of light. We calculate the electric field of an arbitrary

motion point charge, using Lienard-Wiechert potentials [3-4]

$$\mathbf{V}(\mathbf{r},t)=\frac{1}{4\pi\varepsilon_0}\frac{qc}{(rc-\mathbf{r}\cdot\mathbf{v})},\quad \mathbf{A}(\mathbf{r},t)=\frac{\mathbf{v}}{c^2}\mathbf{V}(\mathbf{r},t)$$

and the expression of correspond electric field $\mathbf{E}$

$$\mathbf{E}=-\nabla\mathbf{V}-\frac{\partial\mathbf{A}}{\partial t}$$

Here we skip the detailed gradient calculation process and just quote the finally results [3-4]

$$\mathbf{E}(\mathbf{r},t)=\frac{q}{4\pi\varepsilon_0}\frac{r}{(\mathbf{r}\cdot\mathbf{u})^3}[(c^2-v^2)\mathbf{u}+\mathbf{r}\times(\mathbf{u}\times\dot{\mathbf{v}})]$$

where $\mathbf{u}\equiv c\hat{\mathbf{r}}-\mathbf{v}$

Due to the carrier's velocity is much less than the velocity of light ($\mathbf{u}\cong c\hat{\mathbf{r}}$), we further modify the equation of moving electron induced electric field

$$\mathbf{E}=(e\mathbf{r}/4\pi\varepsilon r^3)+(e/4\pi\varepsilon c^2 r^3)[\mathbf{r}\times(\mathbf{r}\times\dot{\mathbf{v}})] \qquad (3\text{-}1)$$

where r is the distance from the carrier to observation position, ε is the dielectric constant, c is the velocity of light, and $\dot{\mathbf{v}}$ is the acceleration of the carrier. The first term of Eq. (3-1) corresponds to Cloumb field; the magnitude decrease as r^2 and can be ignore at far field. The second term describes the radiation field which is p-wave. Substituting carrier velocity $\boldsymbol{v}$ into current density $\boldsymbol{J}$ = $e\boldsymbol{v}$, the photo-carrier induced radiation term in Eq. (3-1) can be rewritten as

$$\mathbf{E}_\theta=(\sin\theta/4\pi\varepsilon c^2 r)\dot{J}\hat{a}_\theta \qquad (3\text{-}2)$$

where θ is the angle between carrier accelerated direction and observed direction. Eq. (3-2) indicates that radiation field induced by accelerated carriers is proportional to time derivative of photo-carrier generated transient current density and the direction of electric field is p-polarized.

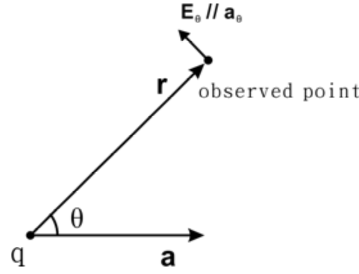

Figure 3-1 The charge accelerated in **a** direction with an angle θ with respect to observation.

Drift Current via Surface Depletion Field

In wide bandgap semiconductors such as GaAs (Eg = 1.43 eV) and InP (Eg = 1.34 eV), due to the discontinuous structure in the air/semiconductor interface, there exists a surface state in the forbidden gap between valance and conduction bands. Due to the band bending to continue Fermi-level on air/semiconductor interface, a depletion region forms, where a surface built-in field exists. The field direction is normal to surface, and strength is a function of Schottky barrier potential and dopant concentration, which is shown in Eq (3-3).

$$E_d(x) = \frac{eN}{\varepsilon}(W - x) \tag{3-3}$$

where ε is material permittivity, N is dopant concentration, and W is the depletion depth which can be written as a function of potential barrier V

$$W = \sqrt{\frac{2\varepsilon}{eN}[V - \frac{kT}{e}]} \tag{3-4}$$

Therefore, surface depletion field induced total transient current is the sum of drift current for electrons and holes,

$$J = J_n + J_p = (en\mu_n + ep\mu_p)E_d$$

For large bandgap semiconductors, the direction of the band bending-induced electric field depends on the dopant types so that the directions of drift current are opposite for *n*- and *p*-type semiconductors. After excitation, the photoexcited carriers in surface

depletion field can be accelerated by an appropriate electric field and the resultant transient electric dipole can lead to the generation of terahertz pulses and the polarization of THz radiation is *p*-polarized for both *p*- and *n*-type semiconductors and THz field strength is proportional to the time derivative of the transient current as the description in Eq. (3-2), that is,

$$E^{\mathrm{THz}} \propto \frac{\partial J(t)}{\partial t} \tag{3-5}$$

Meanwhile, for narrow band gap semiconductors which possess a narrow depletion region near the surface and the so-called the photo-Dember effect dominates the THz emission from them.

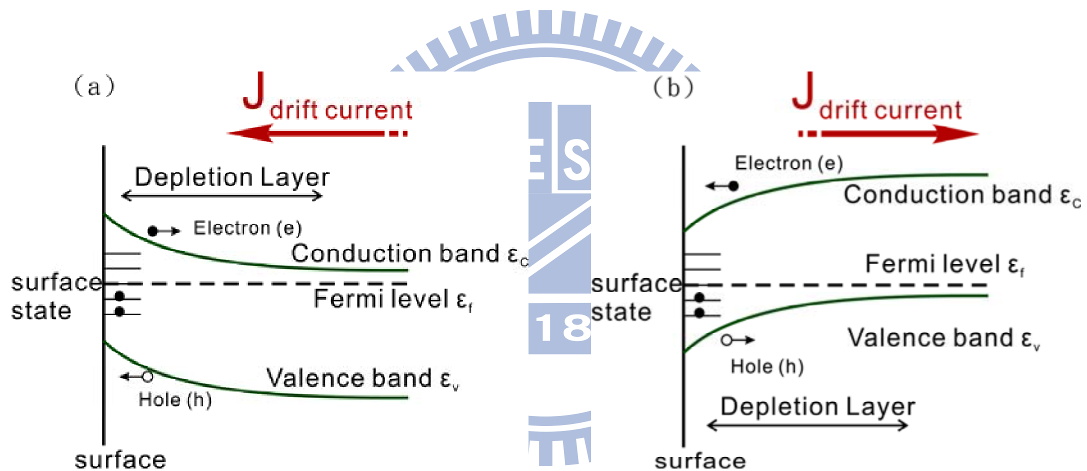

Figure 3-2 Photo drift current via surface depletion field (a) for typical n-type semiconductor (b) for typical p-type semiconductor.

<u>Diffusion Current via Photo-Dember Effect</u>

For the narrow bandgap semiconductors, such as InAs and InSb, the band bending is not significant and for photoexcitation with near IR light, the excess energy of the narrow semiconductor is very large. In addition, the optical absorption length is typically of the order of a few hundred nm. Photoexcitation increases the photoexcited carriers near the surface and then the carriers diffuse into semiconductor. Due to the different diffusion velocity between electrons and holes, the spatial charge separation

can be formed and induces the build-in electric field (or photo-Dember field). The photo-Dember current is the sum of the diffusion current for electrons and holes,

$$J_{\text{diffusion}} = J_n + J_p \sim -eD_e \frac{\partial \Delta n}{\partial x} + eD_h \frac{\partial \Delta p}{\partial x} \tag{3-6}$$

where Δn and Δp are the densities of photoexcited electrons and holes, D_e and D_h indicate diffusion coefficient of electrons and holes, respectively. The diffusion coefficient D is defined by the Einstein relation, $D = k_B T \mu / e$, where μ is the mobility of electrons or holes which can be obtained by Hall measurement. Hence, THz radiation is proportional to the difference in mobility and temperature between the electrons and holes, and the gradient carrier density. Since the mobility of electrons is always greater than that of holes, the photo-Dember current induced THz fields for different dopant semiconductors (n-type or p-type) have the same irradiative direction, which is outward and normal to surface as shown in Fig. 3-3. Therefore, the photo-Dember effect is dominant for THz emission from the narrow bandgap semiconductors with the large mobility ratio of electrons and holes (μ_e / μ_h) and richer excess energy of carriers (T_e) [3-5]. Finally, because of small effective mass and high mobility, the photo-current has fast rise- and decay time character which is benefit to obtaining a broadband THz spectrum.

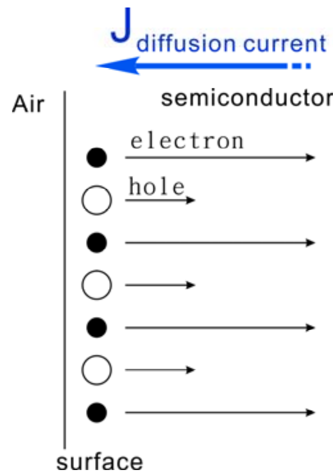

Figure 3-3 Photo diffusion current from different diffusion velocity of electrons and holes.

3-1.2. Instantaneous Nonlinear Polarization (Optical Rectification)

As ultrafast laser excited semiconductor via resonant (above band-gap) or nonresonant (below band-gap) excitation process, because of spatial separation of final electron and hole states, this process leads to an instantaneous polarization $\mathbf{P}_0$ whose second time derivative $\partial^2 \mathbf{P}_0 / \partial t^2$ determines the radiated signal. In general, linear polarization takes place in dielectric material, while nonlinear polarization occurs when nonlinear coefficient $\chi^{(2)}E + \chi^{(3)}E^2 + \ldots$ is comparable to linear coefficient $\chi^{(1)}$ at high excitation density.

In addition to transient current induced by free carriers, the instantaneous polarization from bound charge also contribute THz emission. Free carriers dominate THz radiation at low excitation, while under high-density excitation nonlinear effect become significant and the screening effect of surface electric field occurs via the high density carriers, which results in the decrease of the transient current. According to the excitation density dependence of the temporal wave forms by M. Nakajima *et al* [3-6], the dominant radiation mechanism changes from the drift current, for low density excitation, to the diffusion current and the optical rectification, for high-density excitation. Except for transient current, in this section we focus on the nonlinear optical effect on the THz radiation. Optical rectification can be regards as a second order optical response which includes second harmonic generation, sum frequency generation, and differential frequency generation. For an anisotropic medium, the instantaneous nonlinear polarization in dipole approximation can be expressed by

$$\mathbf{P}_i^{(2)}(\omega_3 = \omega_1 + \omega_2) = \chi_{ijk}^{(2)}(-\omega_3; \omega_1, \omega_2)\mathbf{E}_j(\omega_1)\mathbf{E}_k(\omega_2) \quad (3\text{-}7)$$

THz emission occurs via the differential frequency generation of two identical input optical pulses (that is, $\Omega=\omega-\omega$). Thus, the influence elements of nonlinear polarization are crystal symmetric characters, the polarization of optical pump and crystal orientation. The effective second-order susceptibility $\chi_{ijk}^{(2)\mathrm{eff}}$ can have bulk- ($\chi_{ijk}^{(2)bulk}$) and surface-electric-field induced ($\chi_{ijk}^{(2)\mathrm{SEF}}$) contributions. For the surface-electric-field contribution, we take only the term of the first-order in the expansion and then the effective nonlinear susceptibility becomes.

$$\chi_{ijk}^{(2)\mathrm{eff}}=\chi_{ijk}^{(2)}(\Omega;-\omega,\omega)+3\chi_{ijkl}^{(3)}(\Omega;-\omega,\omega,0)E_z^{\mathrm{surf}} \qquad (3\text{-}8)$$

where $\chi_{ijk}^{(2)\mathrm{bulk}}$ is the intrinsic bulk second-order susceptibility tensor which is determined by the symmetry properties of the bulk crystal and we refer $3\chi_{ijkl}^{(3)}E_z^{\mathrm{surf}}$ to surface-electric-field (SEF) induced effective surface susceptibility. In the following, we will discuss the bulk- and SEF induced second-order optical responses separately. It should be noted here that the calculation that follows is sufficient to describe the process of second harmonic generation, as the only difference is that the polarization of the lattice occurs at the sum frequency ($2\omega=\omega+\omega$), whereas the far-infrared generation occurs at the difference frequency ($\Omega=\omega-\omega$).

Then, by substituting the bulk- (SEF-) susceptibility into nonlinear polarization and applying transformation matrix crystal (surface) coordinate to lab coordinate, we could get bulk- (SEF-) second-order optical response (ex. THz field and SHG).

Bulk Second-Order Optical Response

Bulk optical polarization can contribute to Terahertz emission and SHG from semiconductor surfaces in reflection geometry. The second-order susceptibility tensor is determined by according to crystal bulk symmetry, and then the intrinsic bulk

nonlinear polarization contributed to THz radiation becomes

$$\mathbf{P}_i^{\text{bulk}}(\Omega) = \chi_{ijk}^{(2)\text{bulk}}(-\Omega;-\omega,\omega)\mathbf{E}_j(-\omega)\mathbf{E}_k(\omega) \tag{3-9}$$

The index notations are determined by the crystal coordinate corresponding to crystal orientation. It should be noted that except the radiated frequency there is the same angularly form for second-order polarization such as SHG and THz. Generally, for crystal without inverse symmetry, it is well known that bulk electro-dipole contribution to SHG dominates over any contribution from surface term. Since InN has a wurtzite structure, $\chi_{ijk}^{(2)\text{bulk}}$ has symmetry properties of the 6mm bulk crystal. The nonvanishing $\chi_{ijk}^{(2)\text{bulk}}$ elements in 6mm symmetry can be expressed as $\mathrm{d}_{15} = \mathrm{d}_{24} = \mathrm{a} \cdot \mathrm{d}_{33}$ and $\mathrm{d}_{31} = \mathrm{d}_{32} = \mathrm{b} \cdot \mathrm{d}_{33}$, where a = b = -0.5 in the bound-charge theory [3-7].

Here we use *d* coefficients to simply the expression of electric susceptibility tensor and their relations are $d_{15} = \chi_{xxz}^{(2)} = \chi_{xzx}^{(2)}$, $d_{24} = \chi_{yyz}^{(2)} = \chi_{yzy}^{(2)}$, $d_{31} = \chi_{zxx}^{(2)}$, $d_{32} = \chi_{zyy}^{(2)}$, and $d_{33} = \chi_{zzz}^{(2)}$. Therefore, the bulk susceptibility tensor for 6mm symmetry [3-8] can be written as

$$\chi_{ijk}^{(2)\text{bulk}} = \begin{bmatrix} 0 & 0 & 0 & 0 & d_{15} & 0 \\ 0 & 0 & 0 & d_{15} & 0 & 0 \\ d_{31} & d_{31} & d_{33} & 0 & 0 & 0 \end{bmatrix} \tag{3-10}$$

The bulk susceptibility tensors for *a*- and *c*-plane are the same since both of them have the same bulk symmetry, 6mm. For *a*-plane InN, defining the beam coordinate system as $(\hat{s},\hat{\kappa},\hat{z})$, where $\hat{z}$ is normal to the crystal surface, *s*-axis is on the crystal surface and parallel to an s -polarized pump beam , and $\hat{\kappa} = \hat{z} \times \hat{s}$. The crystal orientation is selected to be $\hat{\mathrm{x}}=[11\bar{2}0]$, $\hat{\mathrm{y}}=[1\bar{1}00]$, and $\hat{\mathrm{z}}=[000\bar{1}]$.

Based on the obtained bulk susceptibility tensor, we can compute the

1896

second-order polarization in the lab coordinate system as a function of azimuthal angle ϕ, pump polarization θ, and incident angle by applying the transformation matrix $A_{s\to l}$ and $A_{c\to s}$ which represent the coordinate transformation from surface to lab and from crystal to surface, respectively.

$$P_{\text{lab}}^{(2)} = A_{s\to l} A_{c\to s} P_{\text{crystal}}^{(2)} \tag{3-11}$$

The optical rectification induced second-order radiation fields are

$$E_s^{(2)} = A_s \Omega L_{\text{eff}} \cdot P_s^{(2)}, \quad E_p^{(2)} = A_p \Omega L_{\text{eff}} \cdot \left[F_s P_z^{(2)} - F_c P_k^{(2)} \right]. \tag{3-12}$$

The coefficients F_s, F_c, A_s, A_p, and L_{eff} in Eq. (3-12) are defined as the projection of the reflected SHG light on the spatial coordinates inside the medium, the corresponding amplitude, and effective phase-matching length, respectively. Their expressions are

$$F_s = \sin\Theta / N, \quad F_c = \sqrt{1 - F_s^2}, \quad A_p = \frac{2\pi T_p}{\cos\Theta}, \quad A_s = \frac{2\pi T_s}{\cos\Theta}$$

where Θ denotes the incident angle of reflection SHG light, and T_p and T_s are the transmission coefficients.

Azimuthal angle dependence of bulk contribution for wurtzite crystal

The generated second-order radiation field for *s*- or *p*- polarized harmonic light due to the bulk anisotropic source as a function of the azimuthal angle become

$$E_{s,p}^{\mathrm{bulk}} = A_{s,p}\Omega L_{\mathrm{eff}}\left[\mathrm{a}_0^{s,p(\mathrm{bulk})} + b_m^{s,p(\mathrm{bulk})}(\cos\phi)^m + c_m^{s,p(\mathrm{bulk})}(\sin\phi)^m\right] \quad (3\text{-}13)$$

the subscript notation indicates *s*- or *p*-polarized bulk electric field. The corresponding coefficients are listed in Table I, and all the distinct elements not shown in the table are zero. The coefficients f_s, f_c, F_s, F_c, t_s, t_p, A_s, A_p, and L_{eff} in Table I are as defined as the projection of fundamental light and reflected SHG on lab coordinated inside medium, the transmission coefficients, the corresponding amplitude, and the effective phase-matching length, respectively. Due to the azimuthal angle dependent experiment of the nonlinear OR induced electric field are selected as $E_{pp}^{(2)}$, $E_{ps}^{(2)}$, $E_{sp}^{(2)}$, and $E_{ss}^{(2)}$ by polarizer [notated as $E_{\mathrm{in,out}}$; for example, E_{ps} represent *s*-polarized electric field irradiated by *p*-polarized fundamental light]. We re-write the expressions of optical rectification induced electric field in Table II. It is noted that ϕ is defined as the angle between the $\hat{k}$ axis and the crystal $[1\bar{1}00]$ axis for *a*-plane InN and the crystal $[11\bar{2}0]$ axis for *c*-plane InN.

Table I. General expressions of bulk contribution to second-order response for *a*- and *c*-plane

Coefficients of bulk second order response from *a*-plane	
E_p^{bulk}	$b_1^{p(\text{bulk})} = A_p \Omega L_{\text{eff}} \left[t_s t_p E_s E_p \{F_c[2f_c(2d_{15} - 2d_{31} + 2d_{33})] - F_s(2f_s d_{15}) \right]$
	$b_3^{p(\text{bulk})} = A_p \Omega L_{\text{eff}} \left[t_s t_p E_s E_p \{F_c[2f_c(4d_{15} + 2d_{31} - 2d_{33})]\} \right]$
	$c_1^{p(\text{bulk})} = A_p \Omega L_{\text{eff}} \left[t_s^2 E_s^2 \{F_c(2d_{15} - d_{33})\} + t_p^2 E_p^2 \{F_s(2f_c f_s d_{15}) - F_c[f_c^2(2d_{15} + d_{31}) + f_s^2 d_{31}]\} \right]$
	$c_3^{p(\text{bulk})} = A_p \Omega L_{\text{eff}} \left[t_s^2 E_s^2 (-2d_{15} + d_{33} - d_{31}) + t_p^2 E_p^2 \{f_c^2(2d_{15} + d_{31} - d_{33})\} \right]$
E_s^{bulk}	$b_1^{s(\text{bulk})} = A_s \Omega L_{\text{eff}} \left[t_s^2 E_s^2 (-2d_{15} - d_{31}) + t_p^2 E_p^2 \left[(f_c^2(2d_{15} - d_{33}) - f_s^2 d_{31}) \right] \right]$
	$b_3^{s(\text{bulk})} = A_s \Omega L_{\text{eff}} \left[t_s^2 E_s^2 (2d_{15} + d_{31} - d_{33}) + t_p^2 E_p^2 f_c^2 (d_{33} - 2d_{15} - d_{31}) \right]$
	$c_1^{s(\text{bulk})} = A_s \Omega L_{\text{eff}} \left[t_s t_p E_s E_p (-4f_c)(d_{15} + d_{31} - d_{33}) \right]$
	$c_3^{2(\text{bulk})} = A_s \Omega L_{\text{eff}} \left[t_s t_p E_s E_p (4f_c)(2d_{15} + d_{31} - d_{33}) \right]$

Coefficients of bulk second order response from *c*-plane	
E_p^{bulk}	$\mathrm{a}_0^{p(\text{bulk})} = A_p \Omega L_{\text{eff}} \left[t_p^2 E_p^2 \{-F_c f_c f_s 2d_{15} + F_s f_c^2 d_{31} + F_s f_s^2 d_{33}\} + t_s^2 E_s^2 \{F_s d_{31}\} \right]$
E_s^{bulk}	$\mathrm{a}_0^{s(\text{bulk})} = A_s \Omega L_{\text{eff}} \left[t_s t_p E_s E_p f_s (2d_{15}) \right]$

Table II. Bulk contribution for different polarization combination from *a*- and *c*-plane.

Coefficients of bulk second order response from *a*-plane	
E_{pp}^{bulk}	$c_1^{pp(\text{bulk})} = A_p \Omega L_{\text{eff}} \cdot t_p^2 E_p^2 \{F_s(2 f_c f_s d_{15}) - F_c[f_c^2(2d_{15} + d_{31}) + f_s^2 d_{31}]\}$ $c_3^{pp(\text{bulk})} = A_p \Omega L_{\text{eff}} \cdot t_p^2 E_p^2 \{f_c^2(2d_{15} + d_{31} - d_{33})\}$
E_{sp}^{bulk}	$c_1^{sp(\text{bulk})} = A_p \Omega L_{\text{eff}} \cdot t_s^2 E_s^2 \{F_c(2d_{15} - d_{33})\}$ $c_3^{sp(\text{bulk})} = A_p \Omega L_{\text{eff}} \cdot t_s^2 E_s^2 (-2d_{15} + d_{33} - d_{31})$
E_{ps}^{bulk}	$b_1^{ps(\text{bulk})} = A_s \Omega L_{\text{eff}} \cdot t_p^2 E_p^2 \left[(f_c^2(2d_{15} - d_{33}) - f_s^2 d_{31})\right]$ $b_3^{ps(\text{bulk})} = A_s \Omega L_{\text{eff}} t_p^2 E_p^2 f_c^2 (d_{33} - 2d_{15} - d_{31})$
E_{ss}^{bulk}	$b_1^{ss(\text{bulk})} = A_s \Omega L_{\text{eff}} \cdot t_s^2 E_s^2 (-2d_{15} - d_{31})$ $b_3^{ss(\text{bulk})} = A_s \Omega L_{\text{eff}} \cdot t_s^2 E_s^2 (2d_{15} + d_{31} - d_{33})$

Coefficients of bulk second order response from *c*-plane	
E_{pp}^{bulk}	$\mathrm{a}_0^{pp(\text{bulk})} = A_p \Omega L_{\text{eff}} \cdot t_p^2 E_p^2 \{-F_c f_c f_s 2d_{15} + F_s f_c^2 d_{31} + F_s f_s^2 d_{33}\}$
E_{sp}^{bulk}	$\mathrm{a}_0^{sp(\text{bulk})} = A_p \Omega L_{\text{eff}} \cdot t_s^2 E_s^2 \{F_s d_{31}\}$
E_{ps}^{bulk}	all coefficients $= 0$
E_{ss}^{bulk}	all coefficients $= 0$

For wurtzite structure, the bulk contribution of second-order response for *a*-plane has one-fold and three-fold symmetry; however, that for *c*-plane is azimuthal angle independent regardless of *s*- or *p*-polarized electric field, as it can be seen in Table I and Table II. There are interesting results that bulk electric dipole for *a*-plane orientation ONLY contributes to azimuthal angle dependence, while that for *c*-plane ONLY contributes azimuthal angle independence.

It should be noted that due to the complicate coefficients it is difficult to organize them to a simple expression of $\cos\theta$, $\cos(3\theta)$, $\sin\theta$ and $\sin(3\theta)$. Hence, in Table I and Table II, we simply describe electric field by a linear combination of $\cos\theta$, $\cos^3\theta$, $\sin\theta$, and $\sin^3\theta$.

Surface-Electric-Field-Induced Second-Order Optical Response

In non-centrosymmetric crystal, the intrinsic surface contribution to optical response is negligibly small compared to the bulk contribution. However, when DC electric field is sufficiently large, the electric-field induced effective second-order optical polarization should be considered. In this session, the surface-electric-field (SEF) induced second-order polarization will be described. As we did in bulk contribution, we start from determining SEF induced second-order susceptibility tensor.

Surface-electric-field-induced effective susceptibility tensor, $\chi_{ijk}^{(2)\mathrm{SEF}}$ is derived from the third-order bulk electric susceptibility tensor

$$\chi_{ijk}^{(2)\mathrm{SEF}} = 3\chi_{ijkl}^{(3)\mathrm{bulk}}(\Omega;-\omega,\omega,0)E_z^{\mathrm{surf}}$$

It means that a surface electric field (E_z^{surf}) breaks the bulk symmetry ($\chi_{ijkl}^{(3)\mathrm{bulk}}$) and creates a new effective susceptibility ($\chi_{ijk}^{(2)\mathrm{SEF}}$). The third-order susceptibility tensor,

$\chi^{(3)}_{ijkl}$ for wurtzite crystals with 6mm symmetry has only 18 nonzero elements: $\chi^{(3)}_{xxxx}$, $\chi^{(3)}_{xxyy}$, $\chi^{(3)}_{xyyx}$, $\chi^{(3)}_{xyxy}$, $\chi^{(3)}_{xzzx}$, $\chi^{(3)}_{xzxz}$, $\chi^{(3)}_{xxzz}$, $\chi^{(3)}_{yyyy}$, $\chi^{(3)}_{yyxx}$, $\chi^{(3)}_{yxxy}$, $\chi^{(3)}_{yxyx}$, $\chi^{(3)}_{yyzz}$, $\chi^{(3)}_{yzzy}$, $\chi^{(3)}_{yzyz}$, $\chi^{(3)}_{zzzz}$, $\chi^{(3)}_{zzyy} = \chi^{(3)}_{zzxx}$, $\chi^{(3)}_{zyyz} = \chi^{(3)}_{zxxz}$, $\chi^{(3)}_{zyzy} = \chi^{(3)}_{zxzx}$.

To properly examine the effective second-order SEF response, we transform the third-order bulk susceptibility tensor to surface coordinate so that the surface field lies along the $\hat{z}$ axis in surface coordinate. Using the transfer matrix, R^{rot}, we expect the form of the effective SEF-induced second-order tensor to be [3-13]

$$\chi^{(2)\text{SEF}}_{\alpha\beta\gamma} = 3E_z^{\text{surf}} \sum_{lmno} R^{\text{rot}}_{\alpha l} R^{\text{rot}}_{\beta m} R^{\text{rot}}_{\gamma n} R^{\text{rot}}_{zo} \chi^{(3)\text{crystal}}_{lmno} \tag{3-14}$$

For *a*-plane InN, it becomes

$$\chi^{(2)\text{SEF}}_{ijk} = \begin{bmatrix} 0 & 0 & 0 & 0 & \partial_{15} & 0 \\ 0 & 0 & 0 & \partial_{24} & 0 & 0 \\ \partial_{31} & \partial_{32} & \partial_{33} & 0 & 0 & 0 \end{bmatrix} \tag{3-15}$$

where ∂_{ij} are constants to represent SEF tensor elements

$$\partial_{15} = 3E_{sz}[\chi^{(3)}_{yyxx} + \chi^{(3)}_{yxyx}]$$

$$\partial_{24} = 3E_{sz}[\chi^{(3)}_{zzxx} + \chi^{(3)}_{zxzx}]$$

$$\partial_{31} = 3E_{sz} \cdot \chi^{(3)}_{xyyx}$$

$$\partial_{32} = 3E_{sz} \cdot \chi^{(3)}_{xzzx}$$

$$\partial_{33} = 3E_{sz} \cdot \chi^{(3)}_{xxxx}$$

For c-plane InN, it is

$$\chi_{ijk}^{(2)\mathrm{SEF}} = \begin{bmatrix} 0 & 0 & 0 & 0 & \partial_{15} & 0 \\ 0 & 0 & 0 & \partial_{15} & 0 & 0 \\ \partial_{31} & \partial_{31} & \partial_{33} & 0 & 0 & 0 \end{bmatrix} \tag{3-16}$$

where

$$\partial_{15} = 3E_{sz}[\chi_{xzxz}^{(3)} + \chi_{xxzz}^{(3)}] \text{ or } 3E_{sz}[\chi_{yyzz}^{(3)} + \chi_{yzyz}^{(3)}]$$

$$\partial_{31} = 3E_{sz} \cdot \chi_{zxxz}^{(3)} \text{ or } 3E_{sz} \cdot \chi_{zyyz}^{(3)}$$

$$\partial_{33} = 3E_{sz} \cdot \chi_{zzzz}^{(3)}$$

We apply the transfer matrix to the effective SEF-induced susceptibility, and evaluate the nonlinear polarization.

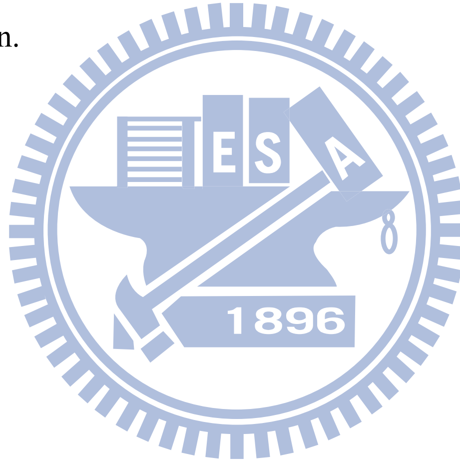

Azimuthal angle dependence of surface contribution for wurtzite crystal

Applying the same coordinate axes as for the bulk case, the anisotropic *s*- or *p*-polarized, SEF-induced radiated fields becomes

$$E_{s,p}^{\mathrm{surf}} = A_{s,p}\Omega L_{\mathrm{eff}}\left[a^{s,p(\mathrm{surf})} + b_n^{s,p}\cos(\mathrm{n}\phi) + c_n^{s,p(\mathrm{surf})}\sin(\mathrm{n}\phi)\right] \tag{3-17}$$

the index notation is same as that for bulk contribution case and the coefficients are listed in Table III. The SEF-induced optical response for different polarization combination is listed in Table IV.

Examining the bulk- and SEF-induced second order electric field, it is not possible to separate the bulk- and SEF-induced contribution for *c*-plane InN due to the identical susceptibility. However, it becomes possible to distinguish them in *a*-plane InN since the built-in electric field distorts the crystal symmetric and creates a new SEF-induced susceptibility [3-15].

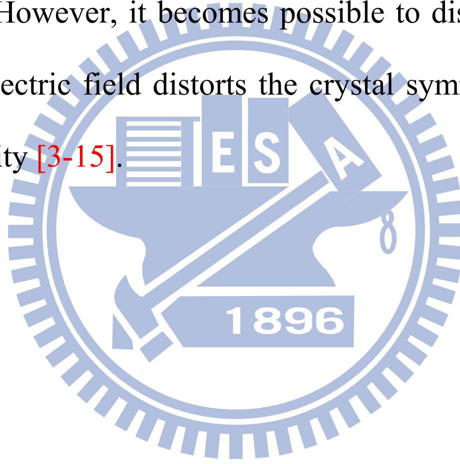

Table III. General expressions of SEF induced contribution to second-order response for *a*- and *c*-plane

	Coefficients of SEF induced second order response from *a*-plane
E_p^{surf}	$a^{p(\mathrm{surf})} = A_p \Omega L_{\mathrm{eff}} \left[t_s^2 E_s^2 \left[1/2 F_s (\partial_{31} + \partial_{32}) \right] + t_p^2 E_p^2 \left[F_s [1/2 f_c^2 (\partial_{31} + \partial_{32}) + f_s^2 \partial_{33}] - F_c [f_c f_s (\partial_{24} + \partial_{15})] \right] \right]$
	$b_2^{p(\mathrm{surf})} = A_p \Omega L_{\mathrm{eff}} \left[t_s^2 E_s^2 \left[F_s [1/2 (\partial_{32} - \partial_{31})] \right] + t_p^2 E_p^2 \left[F_s [f_c^2 1/2 (\partial_{31} - \partial_{32})] - F_c [f_c f_s (\partial_{15} - \partial_{24})] \right] \right]$
	$c_2^{p(\mathrm{surf})} = A_p \Omega L_{\mathrm{eff}} \left[t_s t_p E_s E_p \left[F_s [f_c (\partial_{31} - \partial_{32})] - F_c [f_s (\partial_{15} - \partial_{24})] \right] \right]$
E_s^{surf}	$a^{s(\mathrm{surf})} = A_s \Omega L_{\mathrm{eff}} \left[t_s t_p E_s E_p [f_s (\partial_{15} + \partial_{24})] \right]$
	$b_2^{s(\mathrm{surf})} = A_s \Omega L_{\mathrm{eff}} \left[t_s t_p E_s E_p [f_s (\partial_{24} - \partial_{15})] \right]$
	$c_2^{s(\mathrm{surf})} = A_s \Omega L_{\mathrm{eff}} \left[t_p^2 E_p^2 [f_s f_c (\partial_{15} - \partial_{24})] \right]$

	Coefficients of SEF induced second order response from *c*-plane
E_p^{surf}	$\mathrm{a}^{p(\mathrm{surface})} = A_p \Omega L_{eff} \left[t_p^2 E_p^2 \{ -F_c f_c f_s 2\partial_{15} + F_s (f_c^2 \partial_{31} + f_s^2 \partial_{33}) \} + t_s^2 E_s^2 \{ F_s \partial_{31} \} \right]$
E_s^{surf}	$\mathrm{a}^{s(\mathrm{surface})} = A_s \Omega L_{\mathrm{eff}} \left[t_s t_p E_s E_p \{ f_s (2\partial_{15}) \} \right]$

Table IV. SEF induced contribution for different polarization combination from a- and c-plan

	Coefficients of SEF induced second order response from a-plane
E_{pp}^{surf}	$a^{pp(\text{surf})} = A_p \Omega L_{\text{eff}} \cdot t_p^2 E_p^2 \left[F_s[1/2 f_c^2 (\partial_{31} + \partial_{32}) + f_s^2 \partial_{33}] - F_c[f_c f_s (\partial_{24} + \partial_{15})] \right]$ $b_2^{pp(\text{surf})} = A_p \Omega L_{\text{eff}} \cdot t_p^2 E_p^2 \left[F_s[f_c^2 1/2(\partial_{31} - \partial_{32})] - F_c[f_c f_s (\partial_{15} - \partial_{24})] \right]$
E_{sp}^{surf}	$a^{sp(\text{surf})} = A_p \Omega L_{\text{eff}} \cdot t_s^2 E_s^2 [1/2 F_s (\partial_{31} + \partial_{32})]$ $b_2^{sp(\text{surf})} = A_p \Omega L_{\text{eff}} \cdot t_s^2 E_s^2 [F_s[1/2(\partial_{32} - \partial_{31})]]$
E_{sp}^{surf}	$c_2^{ps(\text{surf})} = A_s \Omega L_{\text{eff}} \cdot t_p^2 E_p^2 [f_s f_c (\partial_{15} - \partial_{24})]$
E_{ss}^{surf}	all coefficients = 0

	Coefficients of SEF induced second order response from c-plane
E_{pp}^{surf}	$\mathrm{a}^{pp(\text{surface})} = A_p \Omega L_{eff} \cdot t_p^2 E_p^2 \{ -F_c f_c f_s 2\partial_{15} + F_s (f_c^2 \partial_{31} + f_s^2 \partial_{33}) \}$
E_{sp}^{surf}	$\mathrm{a}^{sp(\text{surface})} = A_p \Omega L_{eff} \cdot t_s^2 E_s^2 \{ F_s \partial_{31} \}$
E_{ps}^{surf}	all coefficients = 0
E_{ss}^{surf}	all coefficients = 0

Pump polarization dependence for wurtzite crystal

We know the instantaneous second-order polarization is expressed as $P_i^{(2)} = \chi_{ijk}^{(2)} E_j E_k$. Therefore, in order to examine the effect of optical rectification, the dependence on either the effective susceptibility or the electric field driven by the laser pulses should be investigated. The azimuthal angle rotation dependence discussed before shows the contribution of the effective electric susceptibility tensor $\chi_{ijk}^{(2)\text{eff}}$, in which the bulk and surface OR mechanism in THz emission could be investigated. On the other hand, we vary the quantity projection of *s*-polarized and *p*-polarized fundamental beam on sample surface via rotating pump polarization at a fixed incident angle to identify the effect of electric field on THz emission.

The polarization of pump beam was rotated by a half-wave plate, while maintaining the azimuthal angle and incident angle of sample. As discussed in azimuthal angle-dependence experiment, we examined the influence of pump polarization direction on the emission of *p*- and *s*- THz waves. We assumed that the pump beam is composite of *p*- and *s*- polarized electric field with a fundamental frequency, i.e. $\mathbf{E}_p^{\text{pump}} = \mathbf{E}_{\text{pump}}\cos\theta$ and $\mathbf{E}_s^{\text{pump}} = \mathbf{E}_{\text{pump}}\sin\theta$. The linear polarization angle θ is defined as the angle between the linear polarized pump beam and a *p*-polarized pump beam. The photo-carrier generated THz field is independent on pump polarization; however, surface and bulk nonlinear responses are possible proportional to $(E_p^{\text{pump}})^2$, $(E_s^{\text{pump}})^2$ and $(E_p^{\text{pump}} E_s^{\text{pump}})$.

For example, for (100) face of n-InAs, emitted *s*-polarized THz signal E_s^{THz} is proportional to $E_p^{\text{pump}} E_s^{\text{pump}}$, while E_p^{THz} is proportional to a linear combination of $(E_p^{\text{pump}})^2$ and $(E_s^{\text{pump}})^2$, i.e. $E_p^{\text{THz}} \propto c_1 + c_2 \cos(2\theta)$ and $E_s^{\text{THz}} \propto c_3 \sin(2\theta)$ [3-12].

Fig. 3-4 shows the *s*- and *p*-polarized THz field amplitude from (100) n-InAs as a function of pump polarization rotation. The pronounced two-fold symmetry for *s*- and *p*-polarized THz field was interpreted as the polarization rotation symmetric property. The two main contributions to a large offset of *p*-polarized THz field compared to *s*-polarized THz field are transient current and polarization angle independence of OR. The 45 degree angle shift between *s*- and *p*-polarized THz fields is attributed to the difference between polarization dependence of cos(2θ) and sin(2θ).

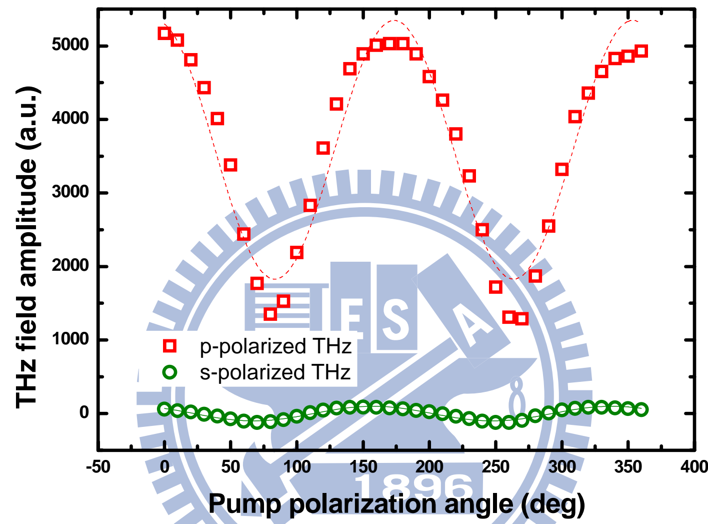

Figure 3-4 Detected *p*- (squares) and *s*- (circles) polarized THz field as a function of the linear pump polarization angle. 0° corresponds to a *p*-polarized pump beam while 90° corresponds to an *s*-polarized beam.

Here we calculated the dependence of pump polarization based on the second-order optical response of bulk and SEF contribution. Since the incident angle and azimuthal angle were fixed in pump polarization rotating experiment, the coefficients of f_s, f_c, F_s, F_c, t_s, t_p, A_s, L_{eff}, and A_p were chosen to be constant during whole process. Substituting the dependence of $\mathbf{E}_p^{\text{pump}}$ and $\mathbf{E}_s^{\text{pump}}$ on the pump polarization rotation angle into Table I and Table III, we obtain the expression of *p*- and *s*-polarized THz field.

For *a*-plane wurtzite crystal,

p- THz: $E_p^{\mathrm{THz}} \propto a_p + b_p \sin(2\theta) + c_p \cos(2\theta)$

s- THz: $E_s^{\mathrm{THz}} \propto a_s + b_s \sin(2\theta) + c_s \cos(2\theta)$

For *c*-plane wurtzite crystal,

p- THz: $E_p^{\mathrm{THz}} \propto a_p + c_p \cos(2\theta)$

s- THz: $E_s^{\mathrm{THz}} \propto b_s \sin(2\theta)$

For *a*-plane orientation, both *p*- and *s*- THz field contain the polarization dependence of sin(2θ) and cos(2θ) and offset signal *a*. Therefore, the discrepancy of polarization dependence for *s*- and *p*- THz is mainly determined by the coefficients of bulk- and SEF-induced contribution. The polarization dependence for *c*-plane wurtzite crystal is similar to (100) face InAs. One can expected that polarization dependent characters for *c*-plane InN will be identical to that for (100) InAs such as large offset for p- THz and phase shift between s- and p-polarization.

Incident angle dependence for wurtzite crystal

The incident angle dependence of transient current induced THz field has been reported [3-25] and the result is shown in Fig. 3-5. At normal incident, the surge current induced THz field is zero since there is no EM field radiated along direction of current. THz amplitude increases as the incident angle increases and has a maximum at near Brewster angle. At the incident angle larger than Brewster angle, THz amplitude is reduced due to Fresnel loss. However, the incident angle can influence Fresnel coefficient in the calculated second-order optical response. Solid line in Fig. 3-5 is the calculated result according to the concept described above [in Table I] and the solid dots are the experimental data in Ref. 3-24, showing the good agreement. Meanwhile, the authors of Ref. 3-24 tried to fit their experimental data based on the d_{eff}^2 coefficient and as it can be seen in Fig. 3-5(b), it only can fit the data around the small angle and is diverged as incident angle is greater than 50 degree. Therefore by taking into account the Fresnel coefficient, we could fit the dependence of THz emission on the full range of incident angle. It is well known that reflection or transmission for *s*- and *p*-polarized light is quite different each other at large incident angle due to Fresnel coefficient. It is the reason why we still can well describe the THz data even when the incident angle is greater than 50 degree.

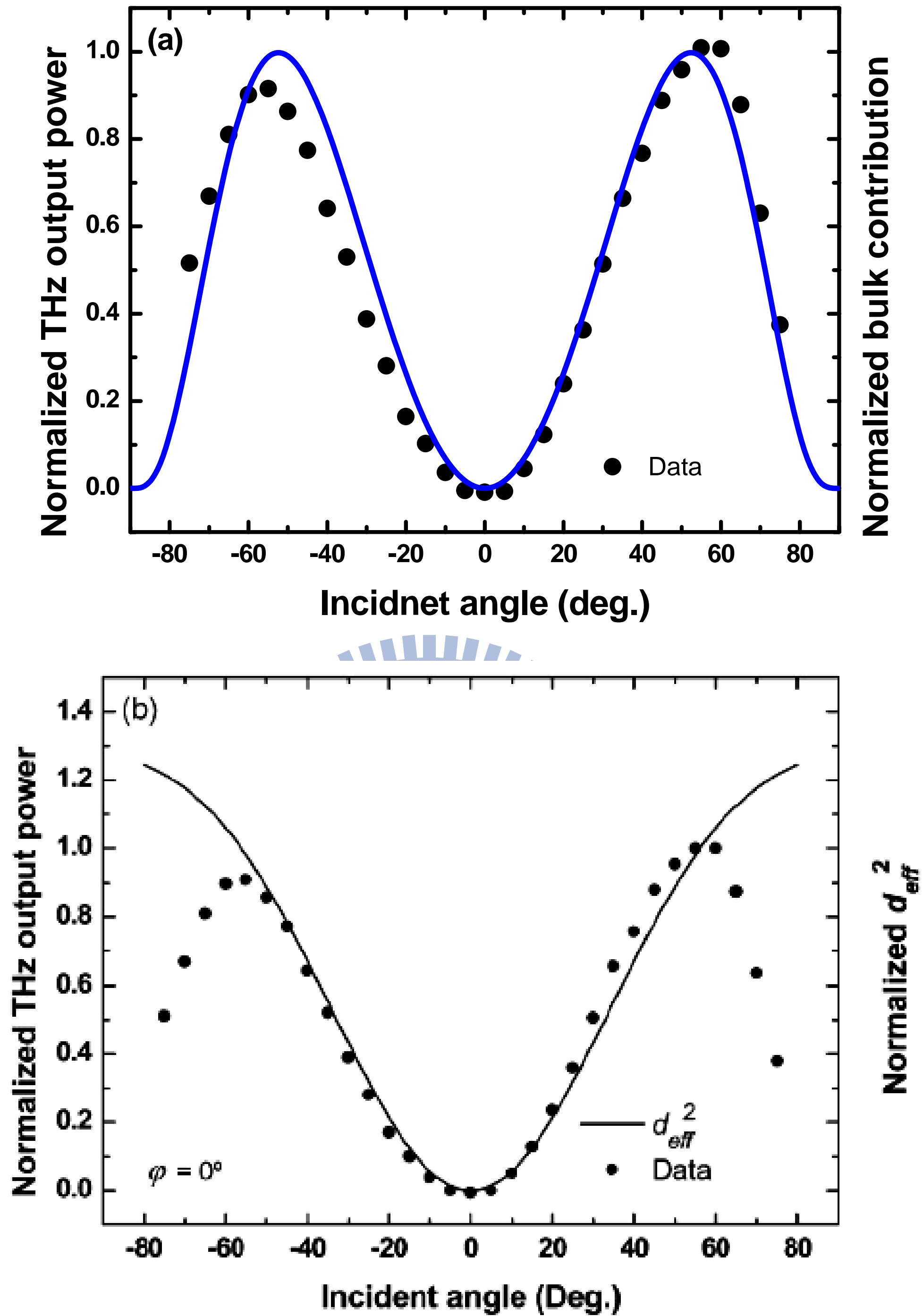

Figure 3-5. Normalized p-polarized THz output power data (dots) [3-24] is fitted by (a) normalized p-polarized bulk contribution (blue solid curves) (b) square of the effective nonlinear coefficient (black solid curves) plotted as a function of incident angle of the pump beam.

3-2. Experimental Setups

In this chapter, we will describe the laser system, EO sampling based THz emission system, reflection second harmonic generation system, and optical pump probe system used in this work.

3-2.1. THz Emission measurement system

The setup of the Electro-Optic THz system is shown in Fig. 3-8. An amplified Ti:sapphire laser providing 50fs, 800nm, 2mJ pulsed at repetition rate of 1kHz is used to drive this system. The linearly *s*-polarized incident beam is divided into three separated beams by two beam splitters. The transmitted beam from the first beam splitter is used for optical pump-terahertz probe study and will be discussed later. The reflected beam from the first beam splitter is divided into the pump beam and the probe beam by the second beam splitter. Polarization of the pump beam is rotated to linearly *p*-polarized by a half-wave plate and is the used to generate linearly *p*-polarized THz pulsed in a semiconductor surface emitter such as InAs at the incident angle of 70 degrees to the surface normal which is close to the Brewster angle. Any reflected laser beam from the emitter is blocked by a teflon sheet which has a high transmission in the terahertz region. The generated THz radiation is collimated and focused onto the sample by a pair of gold-coated off-axis parabolic mirrors with focal lengths of 3 and 6 inches respectively. The transmitted THz radiation is again collimated and focused onto a 2-mm-thick (110) ZnTe crystal for free space electro-optic sampling by another pair of parabolic mirrors with the same focal lengths with previous pair. A pellicle beam splitter which is transparent to the THz beam and has a reflectivity of 5% for 800nm light is used to make the probe beam collinear with the THz beam in the ZnTe crystal. The linear polarization of the probe beam is perpendicular to the polarization of the THz beam and we adjust the

azimuth angle of the ZnTe crystal to achieve the highest modulation efficiency. The linear polarization of the probe beam without being modulated by the THz radiation is converted to circular polarization by a quarter-wave plate; Polarization of the probe beam modulated by the THz radiation is converted to ellipsoid polarization by a quarter-wave plate. A Wollaston beam splitter is used to divide the modulated ellipsoid polarized probe beam into a linear *s*-polarized beam and a *p*-polarized beam. A balanced detector with two silicon photodiodes is used to detect the differential signal between two individual probe beams and the signal is proportional to the THz electric field. A motor stage within the probe beam path is used to scan the delay time between the probe pulse and the THz pulse imposing on the ZnTe crystal to obtain the entire THz time-domain waveform. In order to increase the signal to noise ratio, an optical chopper and a lock-in amplifier are used. The entire THz beam path is also located in a closed acrylic box for nitrogen purge. An example of a terahertz pulse with its corresponding spectrum under humidity of 5% generated by this setup is shown in Fig. 3-9.

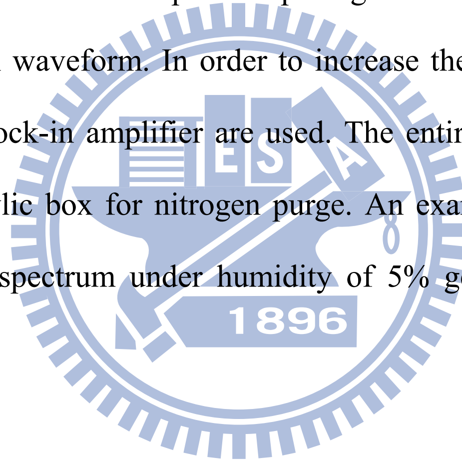

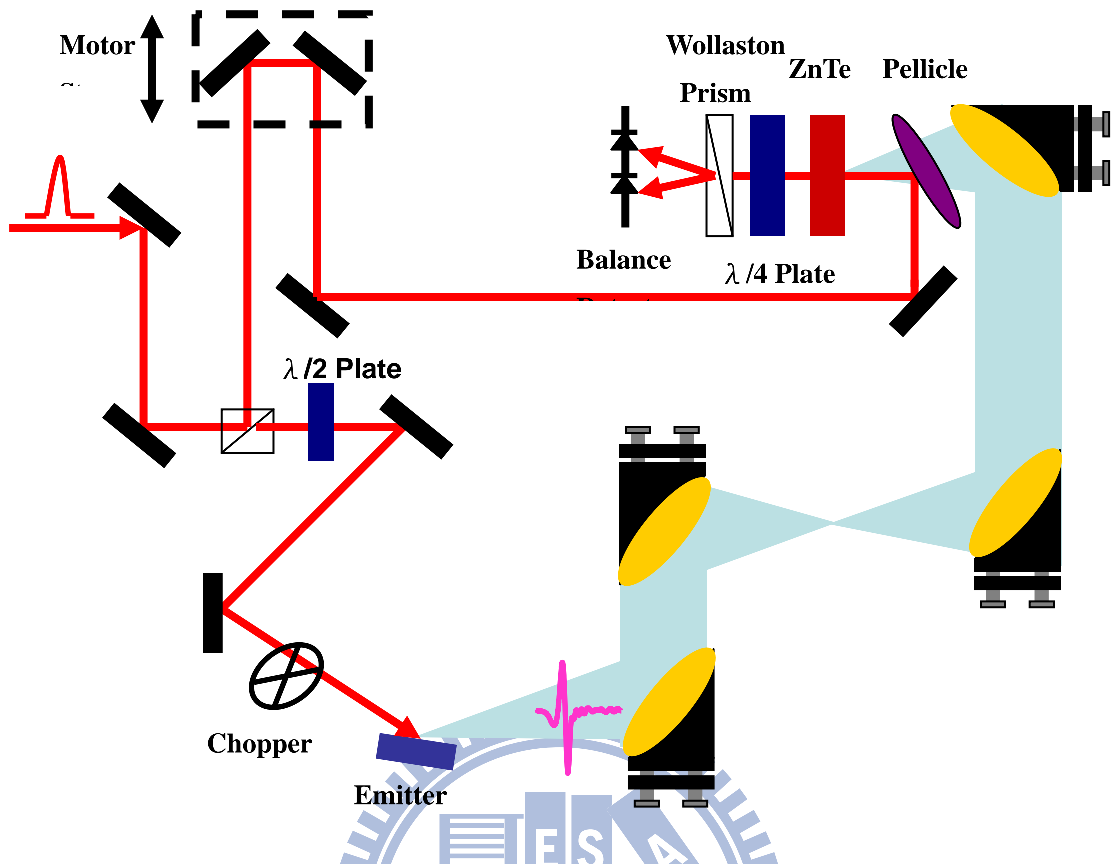

Figure 3-8 Electro-optic THz emission system

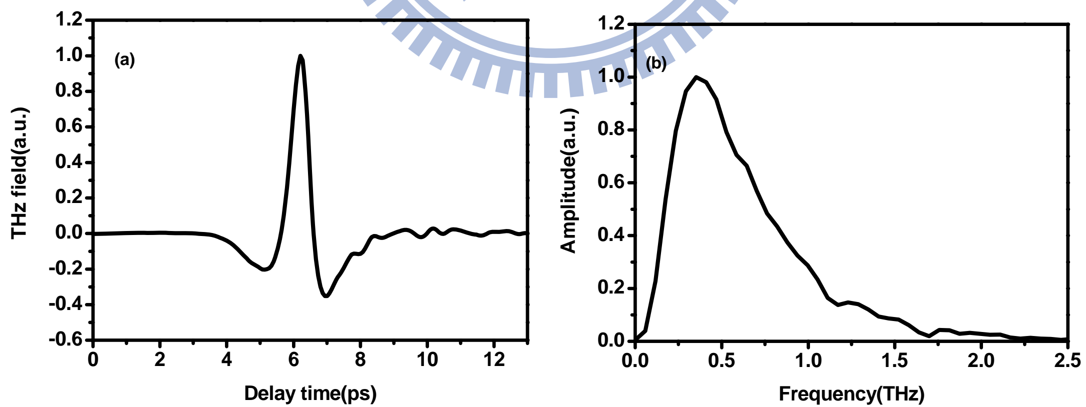

Figure 3-9 THz time-domain (a) waveform and (b) its corresponding spectrum generated by the electro-optic THz emission system using InAs as emitter under humidity of 5%

3-2.3. Reflection Second Harmonic Generation (RSHG) Setups

Fig. 3-10 displays an experimental setup for second harmonic generation from semiconductor surface. Mode-locked Ti:saphire regenerative amplifier is used as pump source filtered by a IR filter and linearly polarized by half wave plate and polarizer. Linearly polarized pump beam is spited to signal arm and reference arm which is used to reduce laser frustration influence. In the reference arm, we choose BBO as NLO crystal to generate 400 nm light as the reference. To efficiently generate SHG, we adjust incident angle to reach phase matching and modify azimuthal angle of BBO to obtain maximum SHG. There is a ND filter in front of BBO and sample to avoid high density damage. Before collecting to Hamamatsu R3896 PMTs, there are bandpass filers and a dichroic mirror to only select 400 nm light. PMTs are connected to multimeters which are monitored by Labview program. The incident angle of focused pump beam is 45 degree and the sample is rotated about its surface normal to examine azimuthal dependent reflection SHG signal. The azimuthal angle dependent results of SHG list in section 3-3.1.

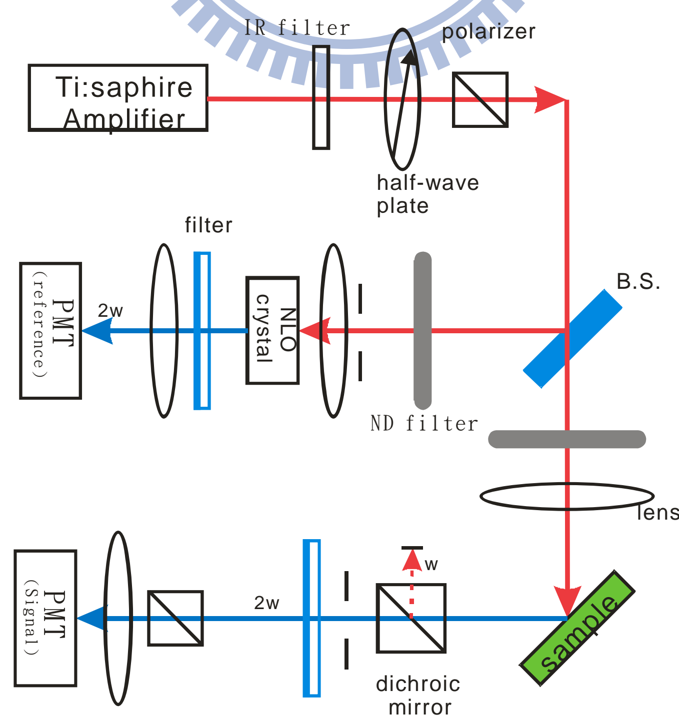

Figure 3-10 Reflection second harmonic generation experiment setup.

3-3. Results and Discussions

First, we discuss the azimuthal angle dependence of RSHG from *a*- and *c*-plane InN surface. Then, the azimuthal angle- and pump polarization- dependent THz field are investigated by EO sampling based THz emission system. Finally we compare THz radiation with SH generation results in summary.

3-3.1. Reflection SH Generation from *a*-plane InN

In the RSHG measurement configuration, since two identical fundamental photons are incident in semiconductor, frequency conversion with the SHG would take place if the momentum and energy are conserved. Since the susceptibility tensor is related to the symmetry of crystal, the effective second-order susceptibility $\chi_{ijk}^{(2)\mathrm{eff}}(\phi)$ in lab coordinate is varied as we rotate azimuthal angle about surface normal. Since susceptibility tensor in lab coordinate also dependent on coordinated transformation, one can expect the function of azimuthal angle dependence is dissimilar for different crystal orientation. Therefore, we are able to distinguish crystal symmetry and orientation via detecting azimuthal angle dependence.

For the measurement, the pump fluence is adjusted to approximately 0.32 mJ/cm^2. The SH intensities are measured as the samples are rotated about their surface normal. The results are shown in Fig. 3-11 for *a*-plane InN and in Fig. 3-12 for *c*-plane InN.

Solid lines are obtained by the bulk electric dipole contribution shown in Table II and they show the excellent agreement with the experimental data. Generally, for crystals without inverse symmetry, it is well known that bulk electro-dipole contribution to SHG dominates any contribution from surface term.

Although *c*- and *a*-plane InN have the same bulk symmetry, 6mm, the pump

beam projection in crystal coordinate are different due to the different orientation. One can predict that samples with different crystal orientation have different azimuthal angle dependence of bulk contribution. The SHG rotational anisotropy result of I_{pp}^{SHG} is named as pp-SHG for the convenience of the following discussion. As expected, the RSHG data for *a*-plane InN show that pp-SHG and ps-SHG are 90 degree phase shifted from ss- SHG and sp-SHG, respectively. The RSHG for *a*-plane InN shows one-fold and three-fold symmetry, while that for *c*-plane InN only has azimuthal angle independent response. Note that both ss-SHG and ps-SHG intensity is zero and the ss-SHG is most sensitive to the symmetry of the surface structure since its polarization combination contains only anisotropic nonlinear susceptibility tensor elements [3-17]. Therefore, in the literature [3-18], to discover the surface configuration of the ZnO thin films, the ss-SHG measurement has been used since the ss-SHG intensity is zero for the bulk of c-plane orientation, as described in Table II.

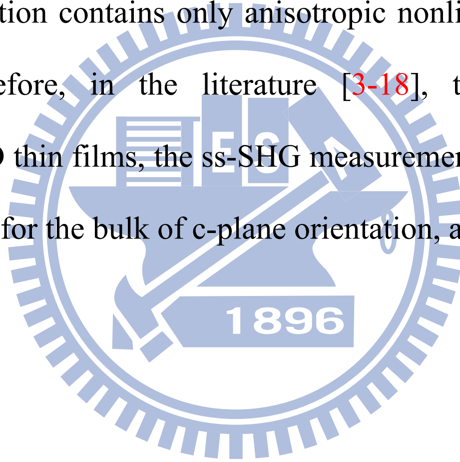

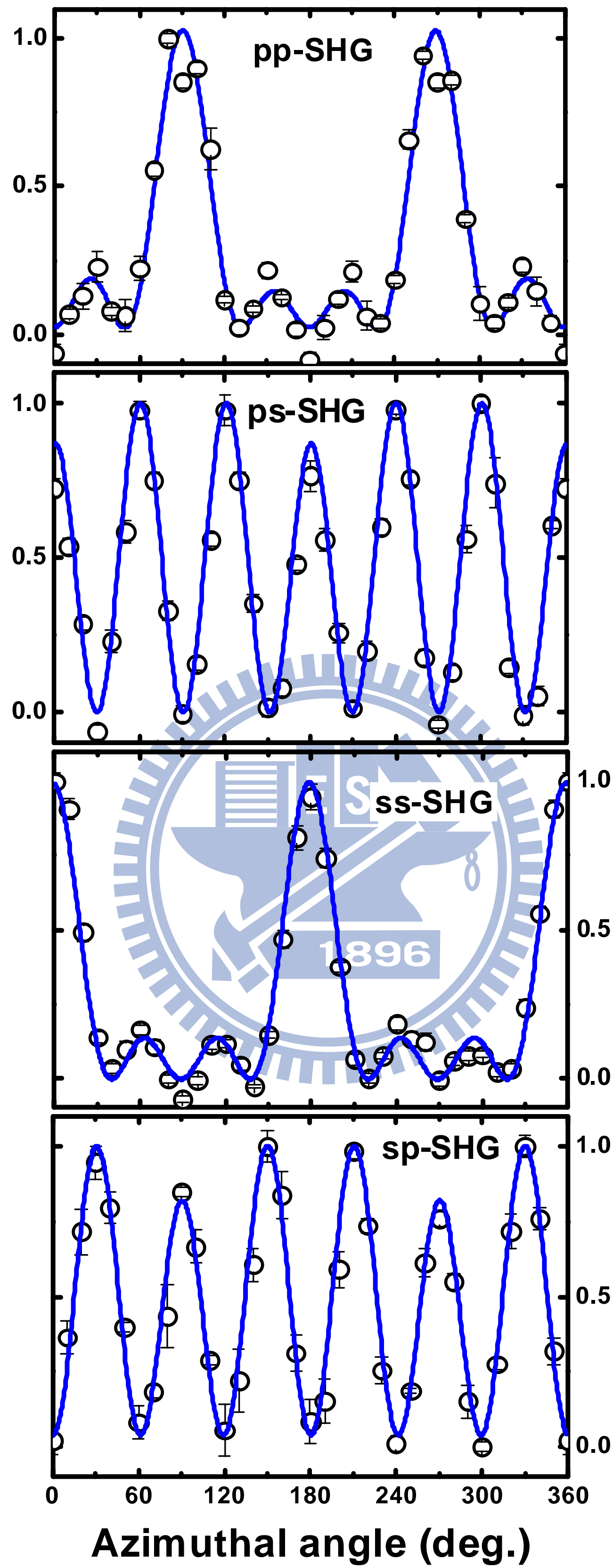

Figure 3-11. Normalized reflection SHG for different polarization combination from *a*-plane InN surface.

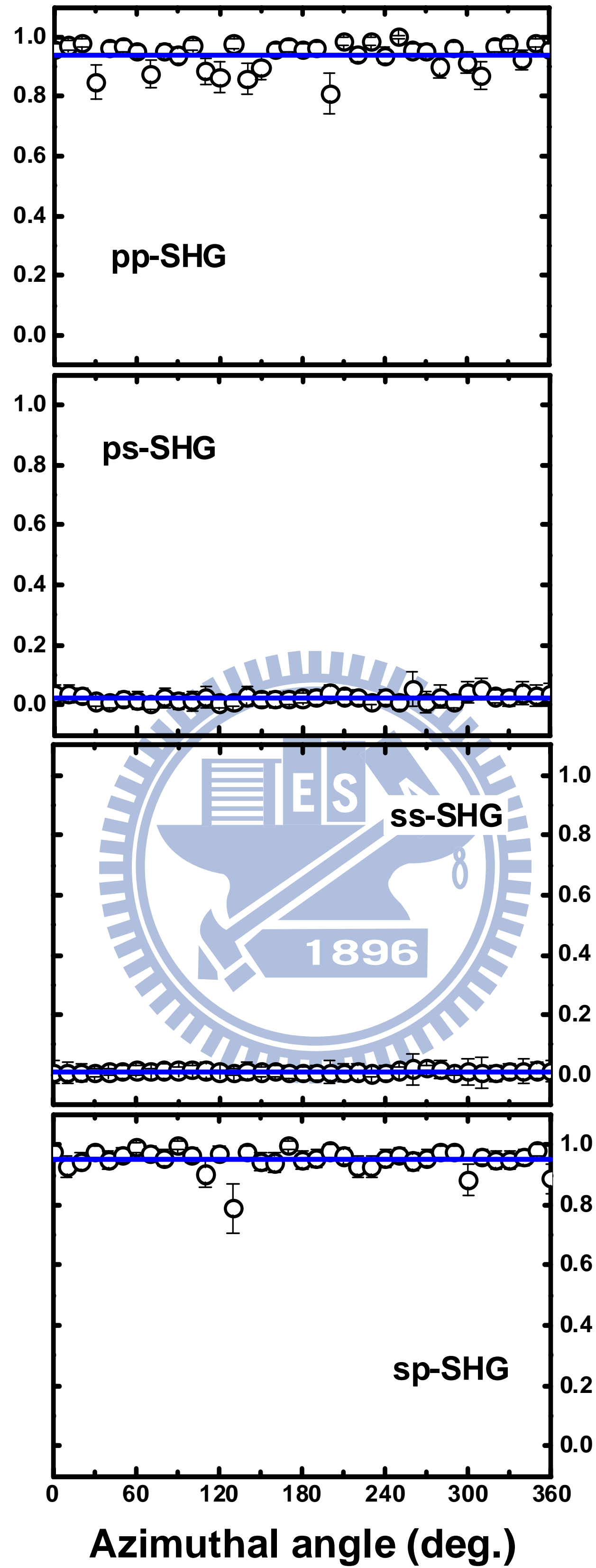

Figure 3-12. Normalized reflection SHG for different polarization combination from *c*-plane InN surface.

Therefore, the azimuthal angle dependencies can be fitted by the relation shown in Table II. For the *a*-plane InN these are $I_{pp}^{\mathrm{SHG}} = [\mathrm{b_1}\sin\phi + \mathrm{c_1}\sin^3\phi]^2$, $I_{ps}^{\mathrm{SHG}} = [\mathrm{b_2}\cos\phi + \mathrm{c_2}\cos^3\phi]^2$, $I_{sp}^{\mathrm{SHG}} = [\mathrm{b_3}\sin\phi + \mathrm{c_3}\sin^3\phi]^2$, and $I_{ss}^{\mathrm{SHG}} = [\mathrm{b_4}\cos\phi + \mathrm{c_4}\cos^3\phi]^2$. The coefficients obtained from the best fitting were $\mathrm{b_1} = 0.11256 \pm 0.00878$, $\mathrm{c_1} = -0.19858 \pm 0.00993$, $\mathrm{b_2} = -0.17288 \pm 0.00586$, $\mathrm{c_2} = 0.23627 \pm 0.00741$, $\mathrm{b_3} = -2.58619 \pm 0.00741$, $\mathrm{c_3} = 3.33633 \pm 0.09824$, $\mathrm{b_4} = 0.10746 \pm 0.00622$, $\mathrm{c_4} = -0.1936 \pm 0.00691$. The coefficient ratios in Table V, we find good agreement with experiments. In Table V, the coefficient *a* and *b* are defined as d_{15}/d_{33} and d_{31}/d_{33}, respectively. Both *a* and *b* used in calculation were -0.5 according to the bond-charge theory [3-7]. The values for the complex refractive index used in the calculations for the optical pump and second-harmonic wavelengths were n = 2.424+*i*0.531 and *N*=2.259+*i* 0.561 [3-19], respectively. The coefficients f_s, f_c, F_s, F_c, t_s, t_p, A_s, L_{eff}, and A_p in Table V are as defined in Ref. 3-10.

In addition, we measured the reflection second harmonic generation from *c*-plane InN, and fitting the data by using $I_{pp}^{\mathrm{SHG}} = \mathrm{a_1}$, $I_{ps}^{\mathrm{SHG}} = \mathrm{a_2}$, $I_{sp}^{\mathrm{SHG}} = \mathrm{a_3}$, and $I_{ss}^{\mathrm{SHG}} = \mathrm{a_4}$. The fitting coefficient were $\mathrm{a_1} = 0.04076 \pm 0.00221$, $\mathrm{a_2} = 5.8\times10^{-4} \pm 7\times10^{-5}$, $\mathrm{a_3} = 0.02589 \pm 0.00143$, and $\mathrm{a_4} = 0.00155 \pm 2.3\times10^{-4}$. The coefficient ratios in Table V for c-plane InN also show the good agreement with experiments.

Table V. The ratios of coefficients of SHG fitting functions are compared calculated with measured values. The ratios are obtained by taking SHG fitting functions and the azimuthal angle dependence of polarization combination radiation fields extracted from Table II.

Expected for *a*-plane InN	Calculated	Measured
$b_1/c_1=[F_s f_s f_c \cdot 2a-F_c(f_c^2(2a+b)+f_s^2 b)]/[-F_c f_c^2(1-2a-b)]$	–0.5784	-0.57 ± 0.01
$b_2/c_2=[f_c^2(2a-1)-f_s^2 b]/[f_c^2(1-2a-b)]$	–0.7814	-0.73 ± 0.09
$b_3/c_3=[-F_c(1-2a)]/[-F_c(b+2a-1)]$	–0.8000	-0.76 ± 0.03
$b_4/c_4=(-2a-b)/(2a+b-1)$	–0.6000	-0.56 ± 0.05
$b_1/b_2=A_p[F_s f_s f_c \cdot a-F_c(f_c^2(2a+b)+f_s^2 b)]/A_s[f_c^2(2a-1)-f_s^2 b]$	–0.7873	-0.73 ± 0.08
$c_1/c_2=A_p[-F_c f_c^2(1-2a-b)]/A_s[f_c^2(1-2a-b)]$	–1.0636	-0.94 ± 0.08
$b_3c_4/b_4c_3=[-F_c(1-2a)](2a+b-1)/(-2a-b)[-F_c(b+2a-1)]$	1.3333	1.36 ± 0.07
$b_1c_3/b_3c_1=[F_s f_s f_c \cdot a-F_c(f_c^2(2a+b)+f_s^2 b)][-F_c(b+2a-1)]/[-F_c(1-2a)][-F_c f_c^2(1-2a-b)]$	0.7230	0.75 ± 0.04
$b_1c_4/b_4c_1=[F_s f_s f_c \cdot a-F_c(f_c^2(2a+b)+f_s^2 b)](2a+b-1)/(-2a-b)[-F_c f_c^2(1-2a-b)]$	0.9640	1.02 ± 0.04
$b_2c_3/b_3c_2=[f_c^2(2a-1)-f_s^2 b][-F_c(b+2a-1)]/[-F_c(1-2a)][f_c^2(1-2a-b)]$	0.9768	0.97 ± 0.12
$b_2c_4/b_4c_2=[f_c^2(2a-1)-f_s^2 b](2a+b-1)/(-2a-b)[f_c^2(1-2a-b)]$	1.3023	1.32 ± 0.03

Expected for *c*-plane InN	Calculated	Measured
$a_2/a_1=0$	0	0.01 ± 0.01
$a_3/a_1=-F_c\left[t_p^2 f_c f_s 2d_{15}\right]+F_s[t_p^2 f_c^2 d_{31}+t_p^2 f_s^2 d_{33}]/F_s t_s^2 d_{31}$	0.6753	0.64 ± 0.14
$a_4/a_1=0$	0	0.02 ± 0.01
$a_2/a_3=0$	0	0.02 ± 0.01
$a_4/a_3=0$	0	0.03 ± 0.02

3-3.2. Azimuthal angle dependence of THz Emission from *a*-plane InN

The azimuthal angle dependence of THz emission from *a*-plane InN film is investigated, which exhibits the influence of optical rectification effect on THz field [3-23]. Fig. 3-13 shows the time-domain waveform and their corresponding amplitude spectrum of THz emission from *a*- and *c*-plane InN. Each sample is excited at the pump fluence of 0.24 mJ/cm^2. It is seen that the amplitude of *p*-polarized radiation component from *a*-plane InN is at least ten times stronger than that from *c*-plane InN. The common contribution of THz emission from InN epilayer is referred to photo-Dember [3-20, 3-21, 3-22] effect due to the narrow electric accumulation layer and large excess energy. However, since the photo-Dember current is proportional to electron mobility and independent to crystal growth direction, its contribution to the radiation from *a*-plane InN (μ = 298 cm^2 /V) is expected to be even smaller than that from *c*-plane InN (μ = 1036 cm^2 /V). Hence, the intense enhancement from *a*-plane InN cannot explained by photo-Dember effect.

The motion of the charge carriers is treated within a Drude-Lorentz approximation, in which the carrier velocity is determined by $d\boldsymbol{v}/dt + \boldsymbol{v}/\tau = (e/m^*)[\mathbf{E}+(\boldsymbol{v}/c)\times\mathbf{B}]$. Here m* and τ are the effective mass and the mean scattering time of the charge carries, respectively. The electric field **E** includes photo-Dember field and in-plane intrinsic electric field $E = E_{\text{p-D.}}\hat{z} + E_{\text{in-plane}}\hat{x}$ ($\hat{x}$ and $\hat{z}$ are in principle plane), and **B** = 0 in our case. Imposing the initial condition $\boldsymbol{v}(t = 0) = 0$, we then find for carrier acceleration induced time-derivative of current density

$$\dot{\mathbf{J}}(t) = e \cdot \mathbf{a}(t) = e^2 / m^* e^{-t/\tau} (E_{\text{depl.}}\hat{z} + E_{\text{in-plane}}\hat{x}) . \qquad (3\text{-}27)$$

For this configuration, the *s*-polarized radiation vanishes (E_s = 0) and the *p*-polarized THz field is given by $E_p(t) \propto \dot{\mathbf{J}} \sin\theta$. As can be seen from Eq. (3-27), the in-plane intrinsic field coverts some of the current initially flowing along the surface

normal $\hat{z}$ to the component parallel to the surface $\hat{x}$. Because of the limited surface emission cone due to total internal reflection, current flowing parallel to the surface radiates much more efficiently than an equivalent current moving perpendicular to the surface [3-16]. Therefore, if the intrinsic electric field is in-plane direction, in-plane current induced THz radiation can escape the emission cone more efficiently. This may explain the drastic power enhancement of the azimuthal angle independent of *p*-polarized THz radiation for *a*-plane InN.

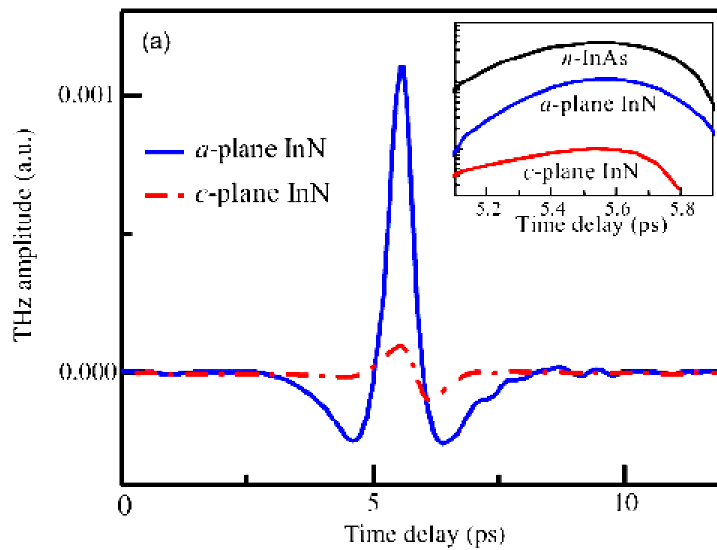

Figure 3-13. THz emission amplitude from *a*- and *c*-plane InN film. Inset shows the comparison between *n*-type InAs and *a*-plane InN.

The apparent azimuthal angle dependence of THz emission has also been observed for *a*-plane InN, as shown in Fig. 3-12, while *c*-plane InN hardly shows the azimuthal angle dependence (Fig. 3-13). The azimuthal angle dependence of THz emission from InN can be well described by the angularly dependence of optical rectification [see Section 3-1.2].

The polarity of photo-carrier-induced THz field reflects the direction of transient current, hence opposite current direction leads to opposite polarity of THz

field. The photo-Dember current always directs to the surface) and we set the polarity of THz field induced by the photo-Dember effect positive. For dielectric materials, the direction of dipole moment is determined by the external electric field. On the other hand, the THz polarity induced by instantaneous polarization can be considered as the direction of dipole moment.

We monitor the peak amplitude of THz amplitude dependent on the azimuthal angle. First, we examined the azimuthal angle experimental data for the *a*-plane in Fig. 3-12. The THz rotational anisotropy result of E_{pp}^{THz} is named as pp-THz for the convenience of the following discussion. Large angularly independent contributions for the pp-THz field and virtually no emission in the ps-THz field have been observed. This may be due to the photo-carrier effect which only generates *p*-polarized THz as discussed before. However, OR effect may partly contribute to the azimuthal angle independence as well. According to the experimental results, pp-THz field has the pronounced azimuthal angle dependence compare to ps-THz field. The fitting results show that azimuthal angle dependence of pp-THz radiation is dominated by bulk electric dipole contribution. According to the calculations, there is no azimuthal angle independence from bulk electric dipole contribution for *a*-plane. In other words, OR effect almost didn't contribute to the azimuthal angle independence of pp-THz field. Then the remaining origin of azimuthal angle independence of pp-THz may be in-plane photogenerated current. For ps-THz, the angularly varied portion is quite small compared to the angular dependence of pp-THz (only 2:100). It means that OR effect of ps-THz can be ignored. We conclude that pp-THz from *a*-InN has a large in-plane current modulated by a pronounced bulk OR and virtually no ps-THz emission.

For *s*-pump arrangement, an asymmetry two-fold symmetric property has been

observed for *p*-polarized THz and there is almost no *s*-polarized THz emission as well. About the polarity of THz, we assumed that the direction of photo-Dember current of InAs is positive, and then we obtain the positive amplitude of pp-THz and negative amplitude of sp-THz field. Since the independent part is impossible to distinguish via fitting, we again start from azimuthal angle dependent fitting results which show that both SEF and bulk contribution to determine the azimuthal dependent data of sp-THz. From the calculation results, we know SEF induced optical polarization has two-fold symmetry; however, bulk optical polarization has both one-fold and three-fold. Due to the bulk contribution, the original two-fold SEF induced THz field becomes asymmetric. According to the dependent fitting results, the angle-independent signal can be attribute to in-plane current and SEF OR since the independent contribution of OR originates in SEF OR for *a*-plane InN.

Here we compare the azimuthal dependence of pp-THz with that of sp-THz. For pp-THz, bulk electric dipole contribution dominates other surface effect; on other hands, both bulk and SEF OR determine sp-THz azimuthal characters. It is interpreted as the physical observation is different for *p*- and *s*-polarized pump beam. Since *s*-polarization is parallel to crystal surface, one can expect that the physical phenomenon of surface effect is most obvious under *s*-polarized pumping. Therefore, sp-THz has a pronounced SEF OR contribution.

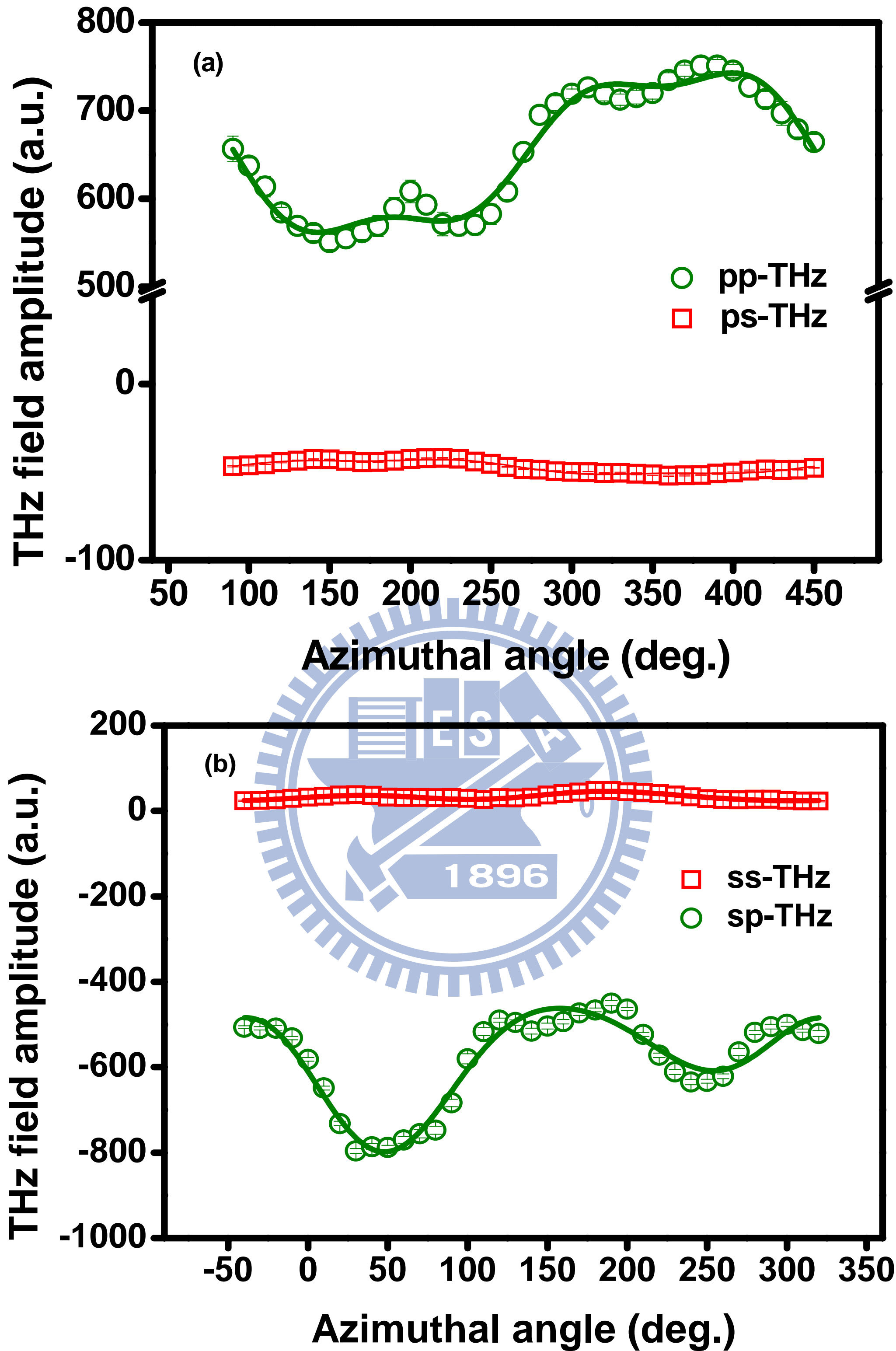

Figure 3-14 Azimuthal angle dependence of THz emission from *a*-plane InN. (a) shows *p*-pump (b) shows *s*-pump THz field. Open circle represents *p*-polarized field and open square represents *s*-polarized field. The solid curves are fits to THz data based on the expectation of linear combination of bulk and SEF induced optical rectification.

Compared to *a*-plane orientation, there is virtually no angular dependence as it is seen in RSHG. This angular independent behavior agrees with our calculated second-order optical response. However, this leads to the difficulty in separating photo-carrier effect and optical rectification from azimuthal angle dependent results. These results of pump polarization dependence show that both photo-carrier and optical rectification contribute to THz emission in *c*-plane orientation.

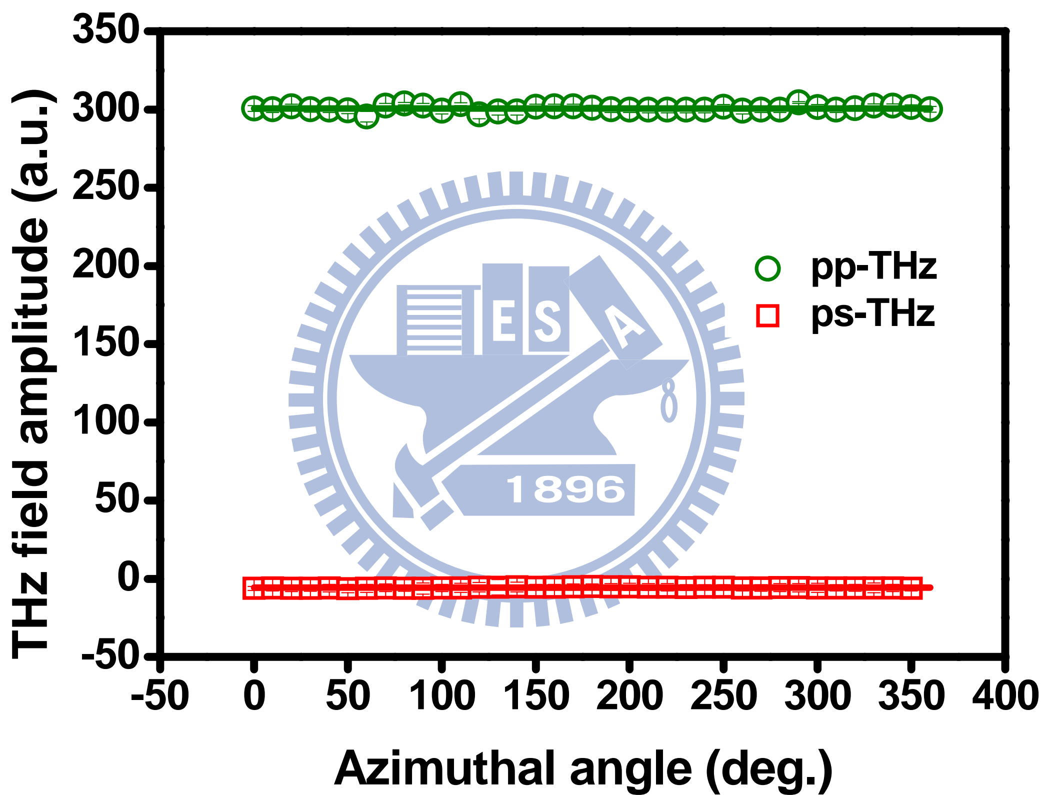

Figure 3-15 Azimuthal angle dependence of THz emission from *c*-plane InN. It shows *p*-pump THz field. Open circle represents *p*-polarized field and open square represents *s*-polarized field. The solid curves are fits to THz data based on the expectation of linear combination of bulk and SEF induced optical rectification.

3-3.3. Pump polarization dependence of THz emission from InN

Fig. 3-16 shows that pump polarization dependence of emitted THz field from *a*- and *c*-plane InN films. Both samples show the large two-fold symmetry when the pump polarization rotates 360 degrees with a pump polarization-independent component. The maximum emission occurs when the pump polarization is *p*-polarized. As we have observed in section 3-1.2, THz emission can be due to either the transient current effect or OR effect. However, only OR effect has the pump polarization-dependent component. The polarity of THz field from *a*-plane is varied when pump polarization is changed from *p*- to *s*-polarization, while the polarity of THz field from *c*-plane remains the positive. Meanwhile, *s*-polarized THz field from both samples is very small compared to *p*-polarized one and since the wire-grid polarizer used to determine the polarization has the extinction ratio of less than 100:1, it may cause the leakage of non-*s*-polarized component to the detector. Therefore, in the following, we will only discuss *p*-polarized THz field responses.

Substituting the refractive indices of fundamental and THz waves into bulk second-order optical response, we obtained the pump polarization dependence of *p*-polarized THz field due to the bulk OR contribution [see Table I]. (Fig. 3-18) For this calculation, the azimuthal angle of the sample is fixed at the one gives the maximum pp-THz.

From the azimuthal angle dependent experimental results, we observe that pp-THz from *a*-InN has a large transient current modulated by the bulk OR-induced current. The pp-THz from *a*-plane InN is large and has positive polarity since it results from the sum of positive bulk OR and positive photo-carrier current.

In the section 3-1.2, we found that sp-THz is due to the summation the transient current effect and bulk- and SEF-induced OR effects. The bulk OR effect has a large negative amplitude contribution at *s*-polarized pump and the combined bulk- and

SEF-induced OR contribution may lead to a negative signal because the positive contribution from photo-carrier current is not large enough at *s*-polarized pump arrangement.

From the azimuthal angle dependent results for *c*-plane InN, we could not separate the photo-carrier effect and OR effect since both of them are azimuthal angle independent for *c*-plane InN. From the pump polarization dependence, we observe a large offset signal modulated by a small dependence for *p*-polarized THz. We attribute the large offset signal to photo-carrier effect which dominates *p*-polarized THz. Due to large photo-carrier effect, although bulk OR is negative at *s*-pump, the whole signal for *p*-polarized THz maintains positive during the rotation of pump polarization.

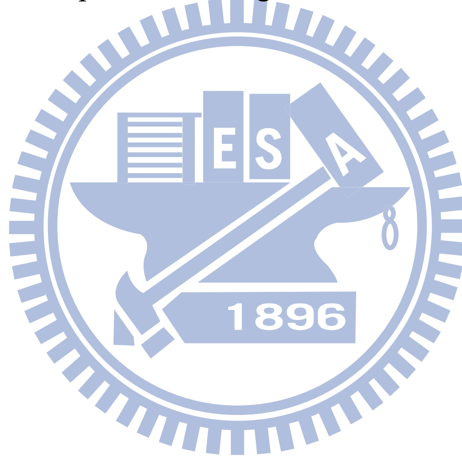

(a)

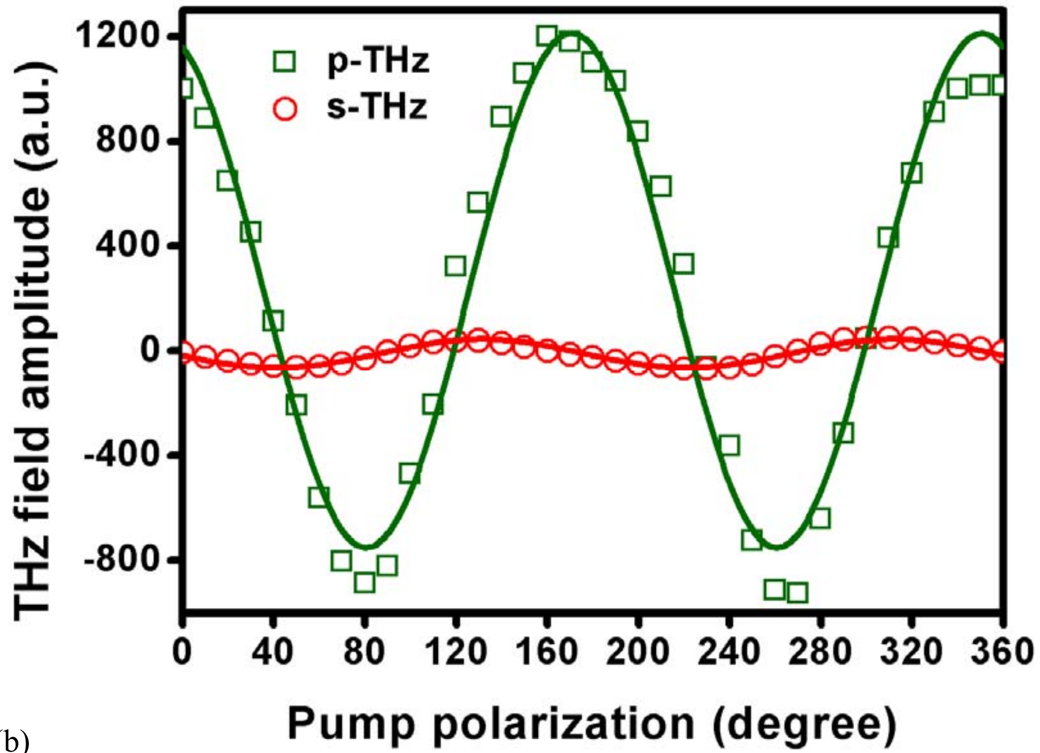

(b)

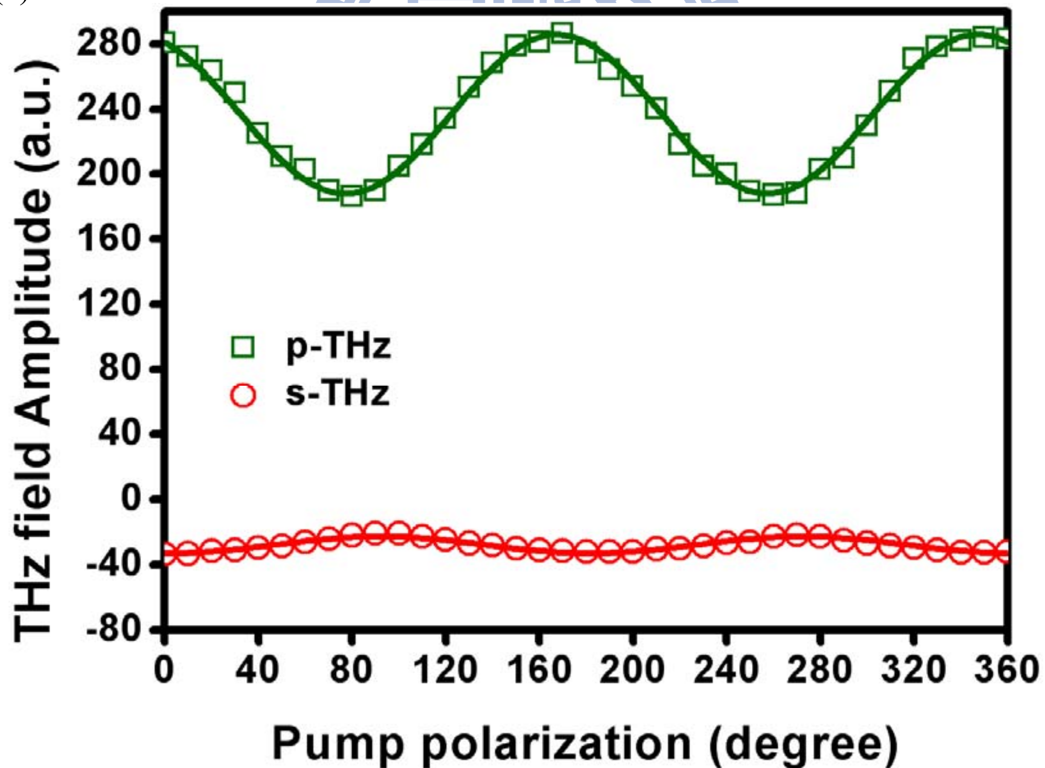

Figure 3-16. Pump polarization dependence of THz field from (a) *a*-plane and (b) *c*-plane InN. The closed square and circle represent *p*-polarized and *s*-polarized THz field, respectively. The solid curves are fits THz data based on pump polarization dependent OR effect.

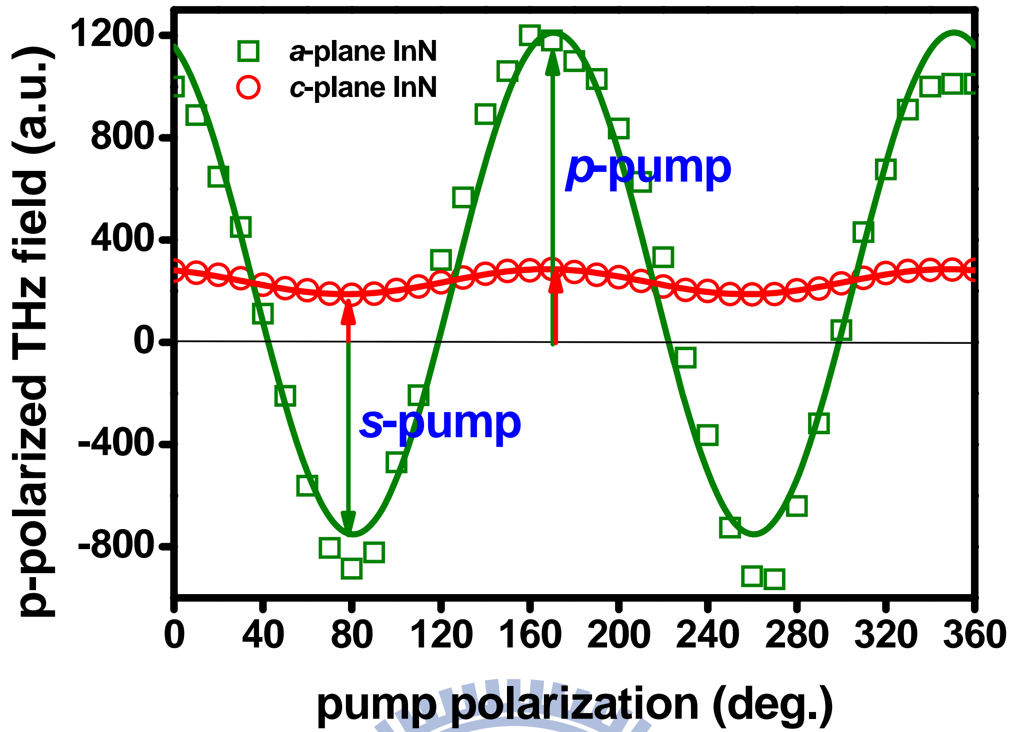

Figure 3-17. Pump polarization dependence of THz field from *a*-plane compared with that from *c*-plane InN.

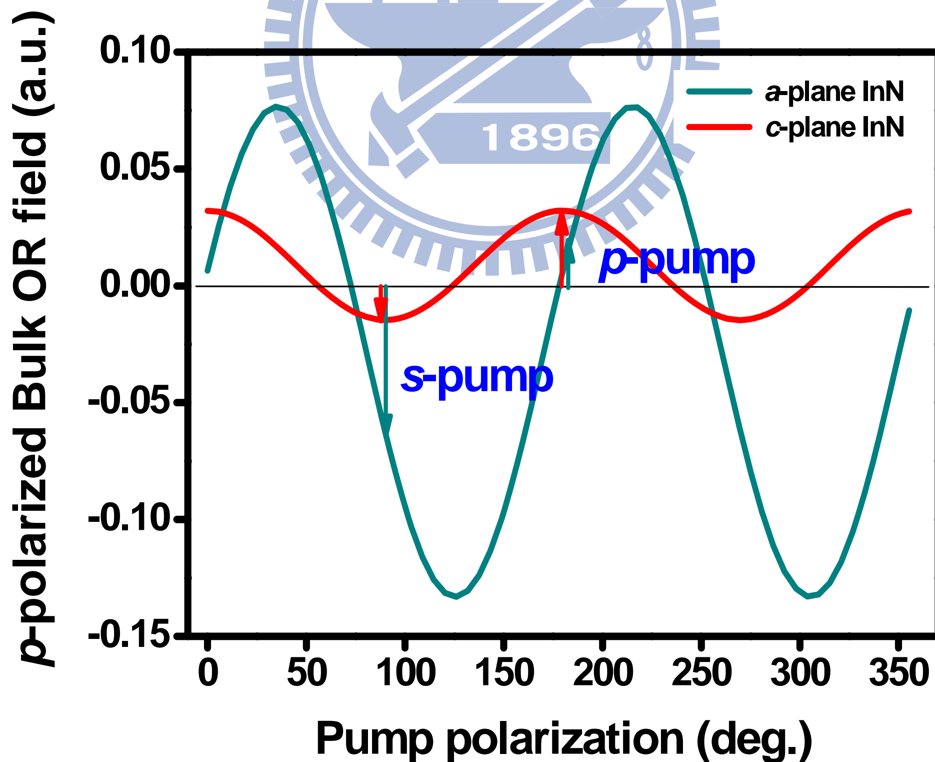

Figure 3-18. The calculated results of pump polarization dependence of *p*-polarized bulk OR contribution from a-plane (red solid line) and c-plane (green solid line) InN based on the angularly dependent functions in Table I.

3-3.4. The comparison between SH generation and THz emission from InN

From the present results, THz field is dominated by both bulk and surface field induced optical rectification effect which dependent on the pump polarization, whereas second harmonic generation is predominated by bulk electric dipole contribution. Based on recent work [3-25], it seems likely that the surface contribution of THz emission results from surface field induced optical rectification rather than a pure surface response. Since optical rectification and second-harmonic generation are complimentary processes, it may seem strange that they are not governed by the same process in the present study.

The several important observations in azimuthal angle dependent experiment are discussed next. First is that THz field is attributed to bulk and surface field induced optical rectification, whereas second harmonic generation is dominated by bulk electric dipole contribution. Second, at high excitation, THz emission from InP [3-26] and InAs [3-9] are dominated by bulk optical rectification and surface electric field induced optical rectification, respectively. For InN film, the main emission mechanisms are photo-carrier effect modulated by bulk and surface field induced optical rectification at such excitation fluence. Additionally, the modulated contribution is determined by pump polarization.

The bulk electro-dipole response contributes to both THz radiation and SHG, which shows second-order susceptibility is important for both of them. Third-order susceptibility in the narrow band-gap III-V semiconductors (InAs and InN) is expected to be strong relative to the larger band-gap semiconductors (InP, GaAs), based on the theoretical calculations by Ching and Huang [3-27]. That is interpreted that THz emission from narrow band-gap semiconductor has significant surface electric field induced optical rectification than large band-gap semiconductor. Jha and Bloembergen [3-28] indicated that the third-order susceptibility is expected to be

dispersive in frequency $\chi^{(3)}(-\omega_4;\ \omega_1,\ \omega_2,\ \omega_3) \propto 1/\omega_1\omega_2\omega_3\omega_4$. This means that the far-infrared response of the third-order susceptibility is significantly larger than the response at the second-harmonic frequency. Therefore, one would expect a much weaker surface electric-field-induced SH intensity in comparison to the electric field induced optical rectification signals due to the dispersion in the third-order susceptibility.

The modulated contribution from InN is referred to the dependence of pump polarization. It may be interpreted as the physical observation is different from *p*- and *s*-polarized pump beam. Since *s*-polarization is parallel to crystal surface, one can expect that the physical phenomenon of surface effect is most obvious under *s*-polarized pumping. Therefore, *s*-pump THz has a pronounced surface field induce optical rectification contribution.

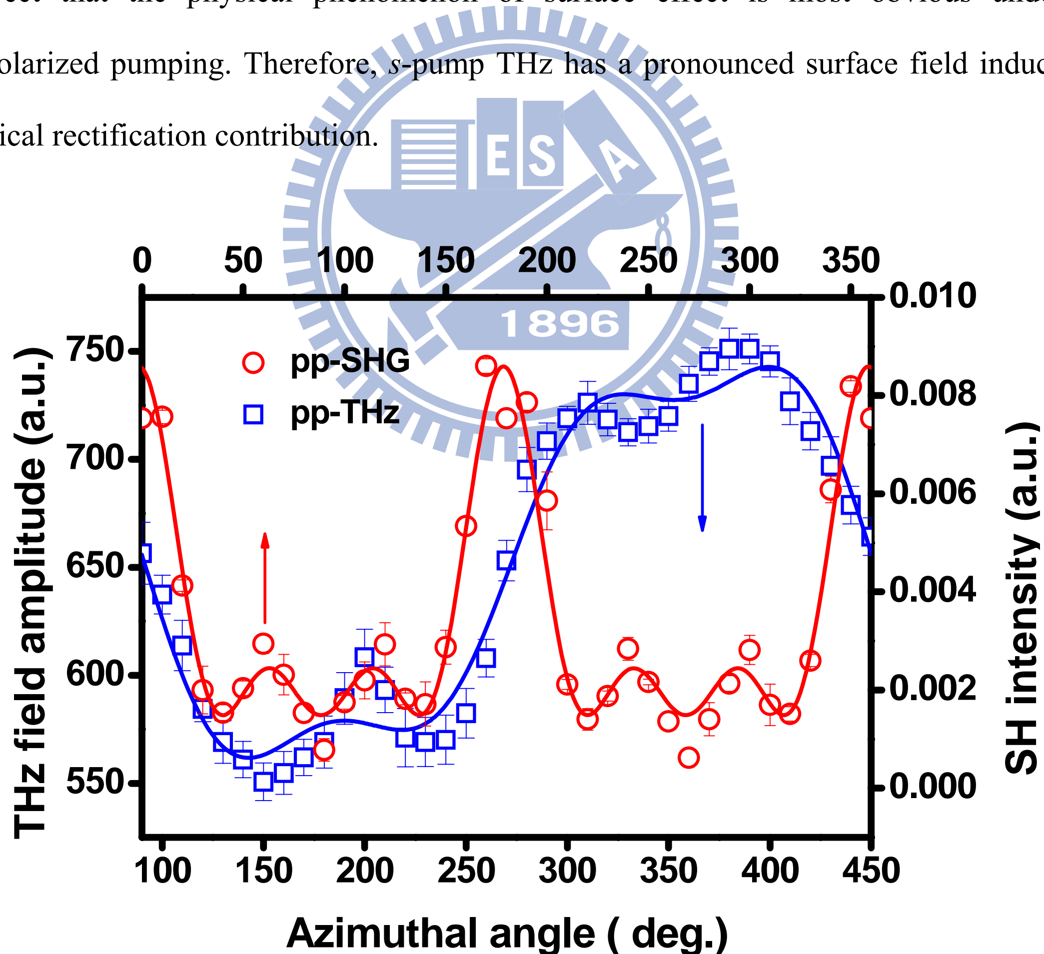

Figure 3-17. The comparison between THz emission and SH intensity from *a*-plane InN. Both of them show the stronger bulk contribution to angular dependence.

References

[3-1] X. C. Zhang and D. H. Auston, "Optoelectronic measurement of semiconductor surfaces and interfaces with femtosecond optics," J. Appl. Phys. **71** 326 (1992)

[3-2] M. B. Johnston, D. M. Whittaker, A. Corchia, A. G. Davies, and E. H. Linfield, "Simulation of terahertz generation at semiconductor surfaces," Phys. Rev. B **65** 165301 (2002)

[3-3] A. Nahata, A. S. Weling, and T. F. Heinz, "A wideband coherent terahertz spectroscopy system using optical rectification and electro-optic sampling," Appl. Phys. Lett. **69** 2321 (1996)

[3-4] David J. Griffiths, "*Introduction to Eletrodynamics*, "3rd Ed., Prentice Hall (1999)

[3-5] Kiyomi Sakai, *Terahertz Optoelectronics*, (Springer-Nict, 2004)

[3-6] M. Nakajima, Y. Oda, and T. Suemoto, "competing terahertz radiation mechanisms in semi-insulating InP at high-density excitation," Appl. Phys. Lett. **85** 2694 (2004)

[3-7] B. F. Levine, "Bond-Charge Calculation of Nonlinear Optical Susceptibility for Various Crystal Structures," Phys. Rev. B **7** 2600 (1973)

[3-8] Robert W. Boyd, "*Nonlinear Optics*," 2nd Ed., Academic Press(2003)

[3-9] M. Reid, I. V. Cravetchi, and R. Fedosejevs, " Terahertz radiation and second-harmonic generation from InAs: Bulk versus surface electric-field-induced contributions," Phys, Rev. B **72** 035301 (2005)

[3-10] W. Hubner, K. H. Benemann, and K. Bohmer, "Theory for the nonlinear optical response of transition metals; Polarization dependence as a fingerprint of the electronic structure at surfaces and interfaces," Phys. Rev. B **50** 17 597 (1994)

[3-11] Q. Chen, M.Tani, Zhiping Jiang, and X.-C. Zhang, "Electro-optic transceivers for terahertz-wave applications," J. Opt. Soc. Am. B **18** 823 (2001)

[3-12] M. Reid and R. Fedosejevs, "Terahertz emission from surface optical rectification in n-InAs," SPIE **5577** 659 (2004)

[3-13] M. Reid and R. Fedosejevs, “Terahertz emission from (100) InAs surfaces at high excitation fluences,” Appl. Phys. Lett. **86** 011906 (2005)

[3-14] T. A. Germer, K. W. Kolasinski, J. C. Stephenson, and L. J. Richter, ”Depletion-electric-field-induced second-harmonic generation near oxidized GaAs (001) surfaces,” Phys. Rev. B **55**, 10 694 (1997)

[3-15] Y. M. Chang, Y. L. Hong, and S. Gwo, ”Direct probe of the built-in electric field of Mg-doped a-plane wurtzite InN surfaces with time-resolved electric field-induced second harmonic generation,” Appl. Phys. Lett. **93** 131106 (2008)

[3-16] J. Shan, C. Weiss, R. Wallenstein, R. Beigang, and T. F. Heinz, ”Origin of magnetic field enhancement in the generation of terahertz radiation from semiconductor surfaces,” Opt. Lett. **26** 849 (2001)

[3-17] O.A. Aktsipetrov, I.M. Baranova, and Y.A. Il’inskii, ”CONTRIBUTION OF SURFACE TO THE GENERATION OF A REFLECTED 2ND HARMONIC FOR CENTRALLY-SYMMETRICAL SEMICONDUCTORS,” Sov. Phys. JETP **64** 167 (1986)

[3-18] K.Y. Lo, Y.J. Huang, J.Y. Huang, Z.C. Feng, W.E. Fenwick, M. Pan, and L.T. Ferguson, “Reflective second harmonic generation from ZnO thin films: A study on the Zn–O bonding, ”Appl. Phys. Lett. **90** 161904 (2007)

[3-19] H. Ahn, C. H. Shen, C. L. Wu, and S. Gwo, “Spectroscopic Ellipsometry Study of Wurtzite InN Epitaxial Films on Si(111) with Varied Carrier Concentrations,” Appl. Phys. Lett. 86 201905 (2005)

[3-20] R. Ascazubi ,I. Wilke, K. Denniston, H. Lu, and W. J. Schaff, “Terahertz emission by InN,” Appl. Phys. Lett. **84** 4810 (2004)

[3-21] G.. D. Chern, E D. Readinger, H. Shen, M. Wraback, C. S. Gallinat, G. Koblmuller, and J. S. Speck, “Excitation wavelength dependence of terahertz emission from InN and InAs, ”Appl. Phys. Lett. **89** 141115 (2006)

[3-22] H. Ahn, Y. P. Ku, Y. C. Wang, C. H. Chuang, S. Gwo, and C. L. Pan, “Terahertz emission from vertically aligned InN nanorod arrays, ”Appl. Phys. Lett. **91** 132108 (2007)

[3-23] H. Ahn, Y. P. Ku, C. H. Chuang, C. L. Pan , H. W. Lin, Y. L. Hong, and S. Gwo, “Intense terahertz emission from *a*-plane InN surface,” Appl. Phys. Lett. **92** 102103 (2008)

[3-24] X. Mu, Y. J. Ding, K. Wang, D. Hena, and Y. B. Zotova, ”Resonant terahertz generation from InN thin films,” Opt. Lett. **32** 1423 (2007)

[3-25] R. Adomavicius, A. Urbanowicz, G. Molis, A. Krotkus, and E. Satkovskis, “Terahertz emission from *p*-InAs due to the instantaneous polarization,” Appl. Phys. Lett. **85** 2463 (2004)

[3-26] P. N. Saeta, B. I. Greene, and S. L. Chuang, “Short terahertz pulses from semiconductor surfaces: The Importance of bulk difference-frequency mixing,” Appl. Phys. Lett. **63** 3482 (1993)

[3-27] W. Y. Ching and M. Z. Huang, “Calculation of optical excitations in cubic semiconductors. III. Third-harmonic generation,” Phys. Rev. B **47** 9479 (1993)

[3-28] S. S. Jha and N. Bloemberge, “Nonlinear optical susceptibilities in Group-IV and III-V semiconductors,” Phys. Rev. **171** 891 (1968)

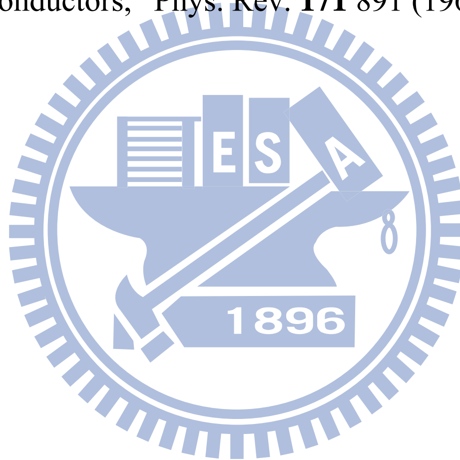

Chap 4. Carrier Dynamics of InN

4-1. Background

4-1.1 Transient Photo-Reflection

Scattering and recombination mechanism affect the dynamics of optically generated carriers in a semiconductor material. Unlike direct current approaches to measure scattering such as DC Hall mobility experiment, the high time resolution of a femtosecond optical pump-probe arrangement can be used to investigate ultrafast carrier dynamics in semiconductor. The transient photo-reflection technique is based on the modulated injection of carriers in a semiconductor sample. The observation of the probe beam reflection yields information about the refractive index of the material. The reflectivity change ΔR depends linearly on the index of refraction change Δn for normal incident:

$$R = \left(\frac{\mathrm{n}-1}{\mathrm{n}+1} \right)^2 \tag{4-1}$$

$$\frac{\Delta R}{R} = \frac{4\Delta \mathrm{n}}{(\mathrm{n}^2 - 1)} \tag{4-2}$$

where n is the index of refraction. The change in the refractive index may depend on several factors [4-1] such as band filling effects, bandgap renormalization and free carrier absorption. In this work the quantitative analysis is limited to the free carrier absorption. The index of refraction change can be modeled through an increase in the plasma frequency [4-2]. This approach gives

$$\frac{\Delta \mathrm{n}}{\mathrm{n}} = \left(\frac{2\pi e^2}{\varepsilon m^* \omega^2} \right) \Delta N \tag{4-3}$$

where ΔN is the density of photoinjected carriers. Therefore,

$$\frac{\Delta R}{R} = \frac{4n}{(n^2 - 1)} \left(\frac{2\pi e^2}{\varepsilon m^* \omega^2} \right) \Delta N \tag{4-4}$$

Here it can be concluded that the transient photo-reflection signal due to free carrier absorption depends linearly on the photocarrier density. Due to this property and because of the high time resolution of the ultrafast pump-probe setup, this technique can be used to perform a direct measurement of the carrier recombination rates in the ultrafast regime.

Several recombination processes can take place in a direct bandgap semiconductor. Non-radiative recombination, interband radiative recombination and Auger recombination are possible. Non-radiative recombination [4-4] is related to localized recombination centers such as impurities, physical defects and surface defects. The non-radiative recombination lifetime can be expressed through the Shockley-Read-Hall theory [4-3] as:

$$\tau_{nr} = \frac{1}{N_{def}\sigma_{def}v_{th}} \tag{4-5}$$

where N_{def} is the density of defects, σ_{def} is their cross section and v_{th} is the carrier thermal velocity. From this equation it can be concluded that for a constant carrier temperature the non-radiative recombination lifetime depends on material and sample parameters (defect density and cross section) and is independent of the photocarrier density.

Interband radiative recombination is proportional to the carrier concentration, and in the case of doped semiconductors the recombination is limited by the minority carrier concentration. The recombination lifetime [4-4] is defined as:

$$\tau_{rad} = \frac{1}{Bn} \tag{4-6}$$

where n is the minority carrier concentration and B is a proportionality constant.

Finally the Auger recombination is the transfer of the electron-hole pair energy to a third carrier. For this reason the Auger recombination time has a higher order dependence on the carrier concentration [4-5]. In summary, the recombination rates

are expressed as:

$$\frac{1}{\tau}=\frac{1}{\tau_{nr}}+\frac{n_0+\Delta n}{B_{rad}}+\frac{(n_0+\Delta n)^2}{C_{Auger}} \tag{4-7}$$

This equation is important because in transient photo-reflection experiments the photoinjected carrier density is high compared to the native carrier density. By observing the lifetime dependence on the photoinjection density, it is possible to distinguish among these recombination mechanisms.

4-1.2 Scattering Processes in Ultrafast Regime

In this section several processes that affect THz emission from optically excited semiconductor surfaces will be presented. Many direct bandgap semiconductors exhibit THz emission when they are optically excited by femtosecond pulses; however, their performance as THz emitters varies dramatically [4-6]. The radiated field strength depends on the electron and hole mobility. In the quasi-classical approach to electron transport in semiconductors, the mobility parameter is used to describe the scattering events taking place in the material. In general, carriers in a semiconductor suffer the following scattering and recombination mechanisms [4-7]:

- Acoustic phonon
- Optical phonon
- Defect related recombination
- Radiative recombination
- Intervalley scattering

Typically in III-V semiconductors, acoustic phonons have relaxation times in the order of tens of picoseconds [4-4]. In the ultrafast regime (picosecond range), where the THz emission process takes place, it is unlikely that these events occur; therefore, this scattering mechanism is immaterial for the THz emission process.

Nevertheless, these events will decrease the mobility measured by DC currents through the Hall effect.

Optical phonon emission occurs at shorter times and this form of scattering does influence the THz emission process [4-8]. Further, optical phonons are expected to play a significant role in scattering in III-V semiconductors due to their polar nature. Table V shows electron-phonon scattering times for some III-V semiconductors.

Non-radiative recombination is a process associated with localized defects. The recombination lifetime for this process is inversely proportional to the defect density as shown in Eq. (4-5). In semiconductors with a high defect density, such as the InN films studied in this work, the defect-related recombination lifetime can have picosecond and sub-picosecond values, and for this reason it negatively influences the THz emission process.

Table V. Electron-phonon scattering times for some III-V semiconductors

Material	Electron-phonon scattering time	LO-phonon scattering time
InN	200 fs	
InP		2.3 ps
InAs	450 fs	1.8 ps
GaAs		2.5 ps

Table VI. Radiative recombination lifetimes for some III-V semiconductors

Material	Rad. Lifetime
InAs	15 μs
GaSb	9 ms
InSb	0.62μs
InN	350μs

Radiative or direct recombination depends on the majority and minority carrier concentrations, but in general the lifetimes for direct recombination in a doped

semiconductor are in the nanosecond range and higher. Table VI shows typical recombination lifetimes for some III-V semiconductors. The table shows radiative recombination lifetimes for intrinsic semiconductors. As the density of carriers increases, the lifetime decreases. However the recombination lifetimes do not reach the ultrafast regime, therefore the probability of a radiative recombination event during the THz emission process discussed in this work is very low.

Intervalley scattering is the process by which excited electrons in the conduction band are transferred to the satellite valleys. The effective mass in those valleys is higher than in the Gamma valley, therefore the total carrier mobility is lower when this process takes place. This process is triggered when carriers have an energy comparable to that of the satellite valley minimum.

Table VII. Satellite valley energy difference for some III-V semiconductors

Material	Γ valley(eV)	L valley(eV)	Difference(eV)
InN	0.68	3.0 – 4.5	1.92 - 4.02
InAs	0.35	1.08	0.73

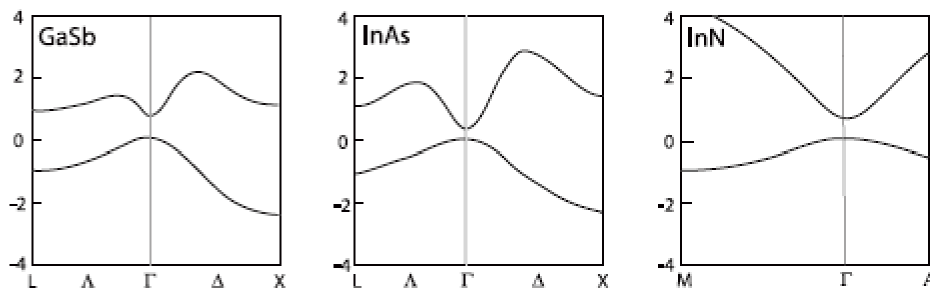

Figure 4-1 Simplified band structure for GaSb [4-9], InAs [4-9] and InN [4-10]. Intervalley scattering is more likely in Gasb than in InAs, for excitation of 1.5 eV photons.

Intervalley scattering has relaxation times in the sub-picosecond scale, and it is especially important in hot carrier diffusion, which is part of the THz emission process from narrow bandgap materials. The relative energies of the L and X valleys with respect to the Γ valley for some III-V semiconductors are shown in Table VII

and in Fig. 4-1. The displacement of electrons into the side-valleys is adverse for THz emission, because the heavier effective mass of the electron in those valleys decreases the total mobility.

From all the processes shown in Fig. 4-2, only optical phonon emission, intervalley scattering and non-radiative defect-related recombination occur on a timescale relevant to the THz emission process.

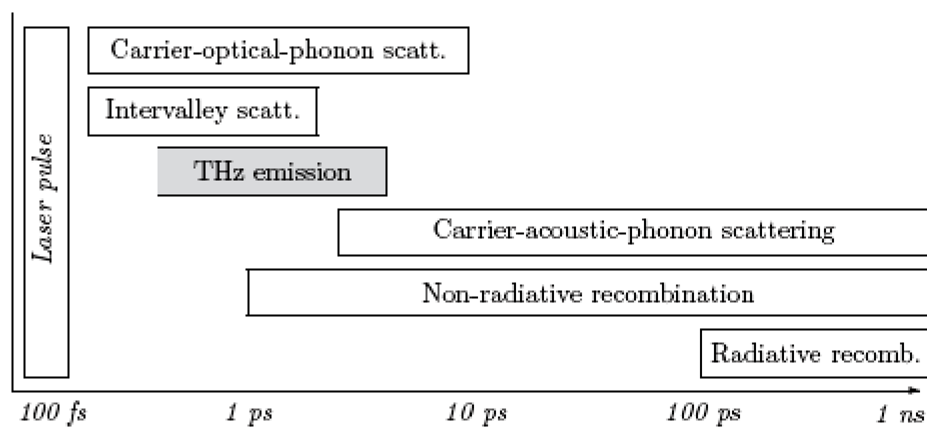

Figure 4-2 Typical timescales of several scattering and recombination mechanisms. Some of these affect the THz emission processes.

4-1.3 Effects of Carrier Generation

4-1.3.1 Band-Filling Effect

The band-filling effect, known as Moss-Burstein effect, describes a decrease in absorption in semiconductor. In a doped semiconductor a relatively small number of electrons can fill the conduction band edge. With the lowest energy states in the conduction band filled, electrons from valence band require more photon energy greater than the bandgap to be optically excited in to conduction band. Hence, there is a decrease in the absorption coefficient at energies above the bandgap.

If parabolic bands are assumed, the optical absorption near the bandgap in a direct-gap semiconductor is given by the square-root law:

$$\alpha_0(E) = \frac{C}{E}\sqrt{E - E_g} \qquad E \ \geq \ E_g$$
$$\alpha_0(E) = 0 \qquad E \ < \ E_g \qquad (4\text{-}8)$$

where $E = \hbar\omega$ is the photon energy, E_g is the bandgap energy, and C is a constant.

In the case of bandfilling, there is a finite probability that a state in the conduction band will be occupied by an electron and /or a state in the valence band will be empty. If we denote an energy in the valence band by E_a and an energy in the conduction band by E_b, then the absorption coefficient of an injected semiconductor is

$$\alpha(N, P, E) = \alpha_0(E)[f_v(E_a) - f_c(E_b)] \qquad (4\text{-}8)$$

where N and P are the concentrations of free electrons and holes, respectively. The bandfilling-induced change in absorption is

$$\Delta\alpha(N, P, E) = \alpha(N, P, E) - \alpha_0(E) \qquad (4\text{-}9)$$

The change in real refractive index n could be obtained by Kramers-Kronig relation

$$n(E) = 1 + \frac{2c\hbar}{e^2}\int_0^\infty \frac{\alpha(E')}{E'^2 - E^2}dE' \qquad (4\text{-}10)$$

The change in absorption and refractive index due to bandfilling has evaluated [4-11].

4-1.3.2 Band-Gap Renormalization

The basic mechanism is that injected electrons will occupy states at the bottom of the conduction band. If the concentration is large enough, the electron wave functions will overlap, forming a gas of interacting particles. The electrons will repel one another by Coulomb forces. In addition, electrons with the same spin will avoid one another for statistical reasons. The net result is a screening of electrons and a decrease in their energy, lowering the energy of the conduction band edge. A similar correlation effect for holes increases the energy of the valence band edge. The sum of these effects is bandgap shrinkage. Shrinkage effects are determined by free carrier density. The free carrier concentration dependent expression for bandgap shrinkage is

$$\Delta E_g(N) = \frac{\kappa}{\varepsilon_s}\left(1 - \frac{N}{N_c}\right)^{1/3} \tag{4-11}$$

where κ is a fitting parameter ε_s is the relative static dielectric constant, and N_c is the critical concentration of free carriers (electrons or holes).

The change in absorption due to shrinkage is predicted to be

$$\Delta\alpha(N,E) = \frac{C}{E}\sqrt{E - E_g - \Delta E_g(N)} - \frac{C}{E}\sqrt{E - E_g} \tag{4-12}$$

As with bandfilling, the change in refractive index was calculated by applying the Kramers-Kronig relation to the $\Delta\alpha$. The refractive index change due to bandfilling also has calculated in Ref. 4-11.

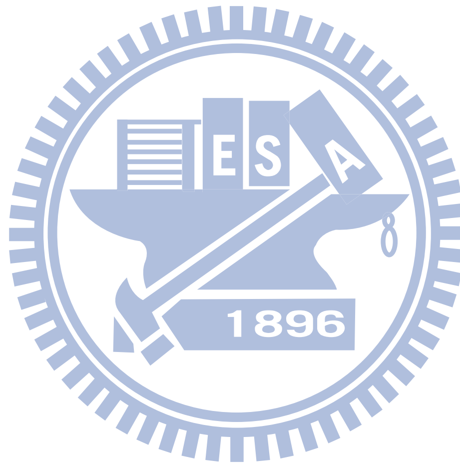

4-2. Experimental Setups

The infrared optical pump probe arrangement is shown in Fig. 4-3. The Ti:sapphire regenerative amplifier laser (Spitfire) is split by 70:30 beamsplitter. The stronger laser beam is used as pump beam excited on sample with an incident angle 10 degree and focused by a lens (f = 100 mm). An optical chopper was used to modulate the pump beam at 150Hz to improve the signal-to-noise ratio. Another weaker laser pulse is used as probe beam focused on sample (f = 50 mm) with incident angle 45 degree and examined the magnitude by Si-diode detector. To reduce the influence of laser frustration, the reference beam is focused on another Si-diode detector. The time resolved photoreflection is obtained by a time delay between pump and probe beam. The polarization of the pump beam is parallel to the plane of incidence and perpendicular to the probe beam polarization to avoid coherent interference. In order to study the dependence of photoreflection signal with optical pump power a variable neutral density filter was used.

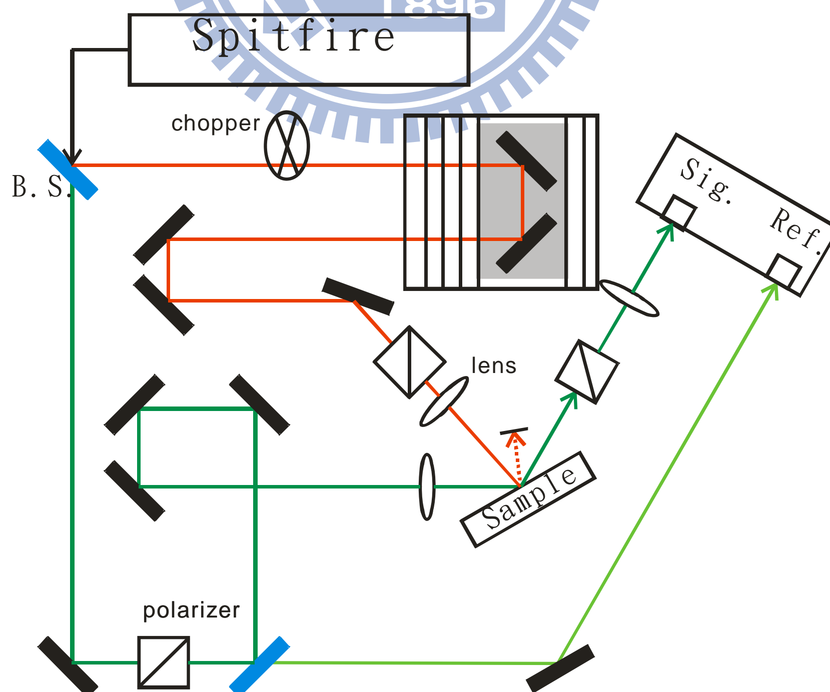

Figure 4-3. The schematic of optical pump probe system.

4-3. Results and Discussions

4-3.1 Fluence Dependent Carrier Dynamic in InN Film and Nanorod

Transient photoreflection was investigated with an optical pump-probe arrangement. The samples are excited with a focused pump beam (diameter ~500 μm) at 800 nm in degenerated pump-probe configuration. The polarization of the pump beam is parallel to the plane of incidence and perpendicular to the probe beam polarization whose fluence is adjusted to be more than ten times smaller than pump beam. The photoexcited transient reflection is generally described by a variation of complex refractive index through several effects such as band-filling (BF), band-gap renormalization (BGR), free carrier absorption, and carrier recombination. Our interpretation of the temporal evolution of the transient reflection of InN follows the interplay of photoinduced absorption and band filling.

The time evolution of normalized transient reflection change ($\Delta R/R_0$) of InN epilayer is shows in Fig. 4-4. The reflectivity change signal is characterized by an initial sharp drop, followed by a quick rise and a second much slower decay of the reflectivity.

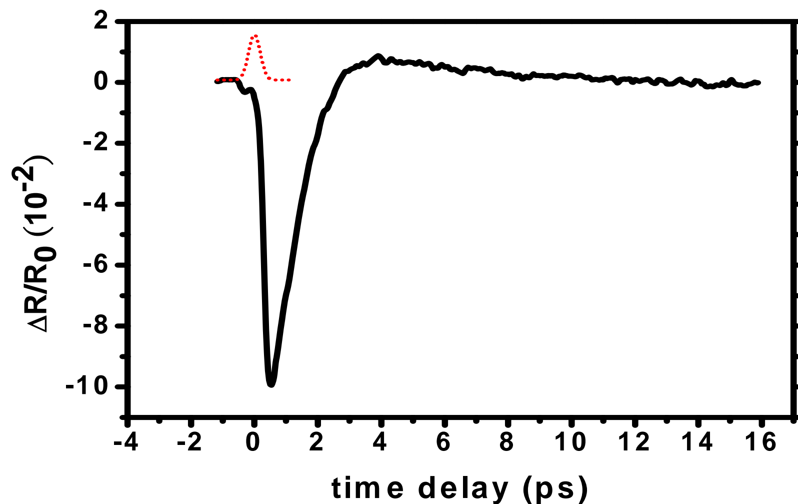

Figure 4-4. The solid line indicates transient photo-reflectivity of undoped InN epilayer at pump fluence 0.509 mJ/cm^2. The zero-delay time is determined by autocorrelation.

We consider the initial fast decrease as the photoinduced absorption. It is known that c-plane InN has strong electron accumulation at surface layer. The spatial dependence of the band bending is described by a potential, $V(z)$ which is given by the solution of the Poisson equation within the modified Thomas-Fermi approximation. As shown in Fig. 4-5, the surface Fermi level of InN was found, from the charge-profile calculation, to be ~1.6 eV above the valence band maximum (E_v) [4-12]. Therefore, intrinsic electrons prefer to locate in surface accumulation layer and to distribute above E_v ~1.6 eV. Although the optical penetration depth of InN at 800 nm is about 150 nm, the most electrons are initially accumulated at surface accumulation layer (<10 nm) due to the band bending. The transient reflectivity change may be related to the surface electrons distribution. The photoinduced absorption (PA) above E_v ~1.5 eV has been observed for InN nanowire [4-13] and rich-In $In_{0.89}Ga_{0.11}N$ epilayer [4-14].

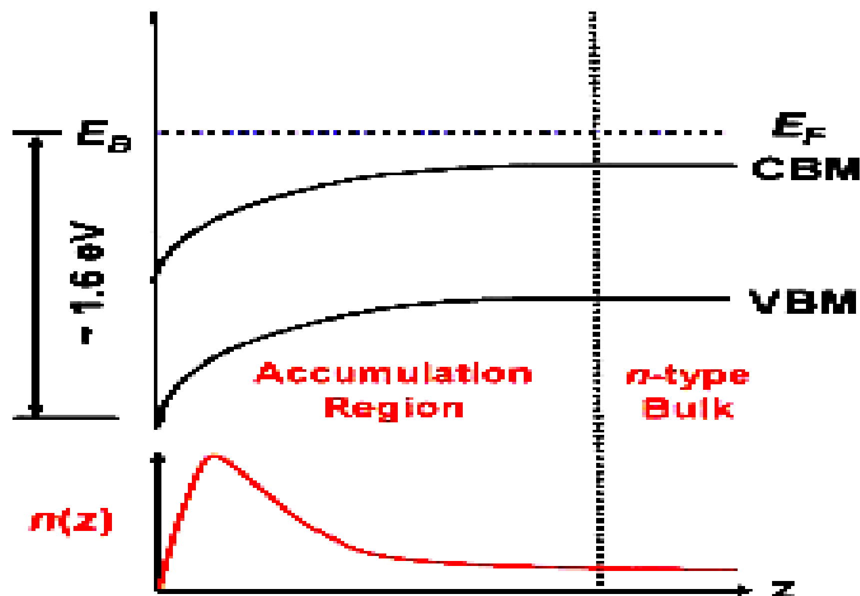

Figure 4-5. The conduction and valence band edges (E_c and E_v, solid lines) and the Fermi level (E_F, dashed line) in the near-surface region of c-plane InN. [4-17]

In this work, we monitor the carrier dynamics at photon energy 1.55 eV (800 nm) which is close to the surface Fermi level. Initially, pump beam excites the carriers to conduction band and fill the states near to Fermi level. Meanwhile, photoinduced absorption at this probe wavelength occurs, which increases absorption of probe beam and results in reflectivity decrease. The reflectivity drop time is limited by system resolution (or laser pulse width ~200 fs). However, due to the high accumulation of the carriers at these energy states, the band filling bring the signal to positive values. After that, the signal is recovered toward equilibrium within 16 ps. From fitting results, since this time constant (~3.5 ps) of InN epilayer is independent to photoexcited carrier density similar to the results of Ref. 4-14 and 4-15, we conclude that it is defect-related recombination time. Hence, as kinetic energy relaxes, carriers may be trapped by defect or surface state.

InN epilayer and nanorods were photoexcited at the range from 0.254 to 0.509 mJ/cm^2. The fluence dependent time constant is extracted via fitting by dual exponential function convoluted with system resolution. For InN epilayer, the absolute reflectivity change is plotted in log-log scale as linear dependent on the fluence. The negative amplitude displays rapidly increase than positive amplitude and the ratio of them shows that at high fluence PA begin to dominate the signal at near zero time delay. The cooling time increases as the fluence increases, which reveals hot carrier relaxation process. The carrier lifetime independent on the fluence is considered as defect-related recombination time.

The time evolution of InN LT nanorods is similar to that of epilayer within 3 ps. A prolong relaxation time (>100 ps) is observed for nanorods. It may be due to the high surface-to-volume ratio for nanorods and the reduction of carrier diffusion rate near the surface. This abnormally long relaxation time for nanorods was also observed for optical-pump THz-probe measurement [4-16].

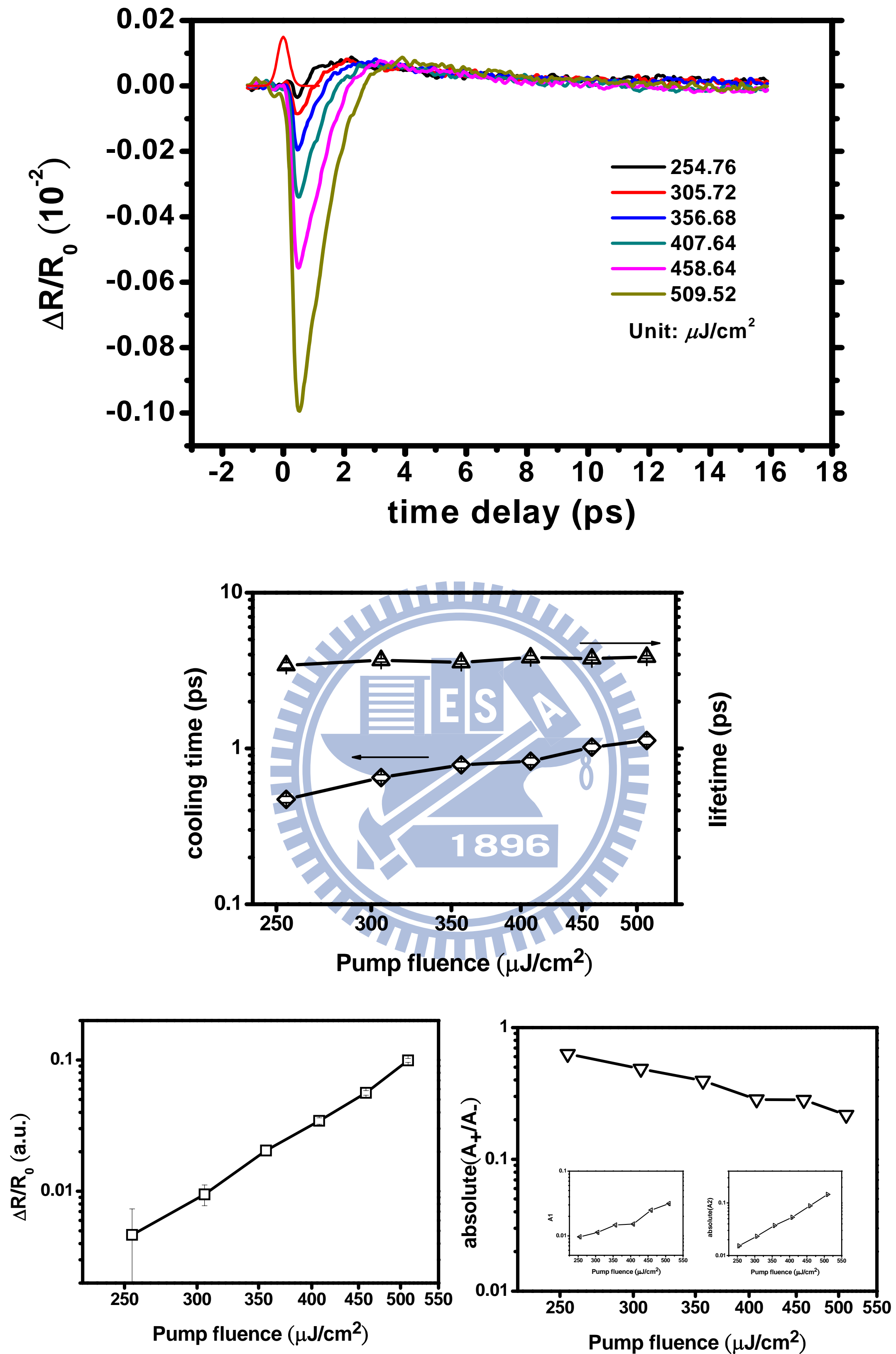

Figure 4-6. The time evolution of transient reflectivity change of InN epilayer and the ultrafast carrier dynamic information.

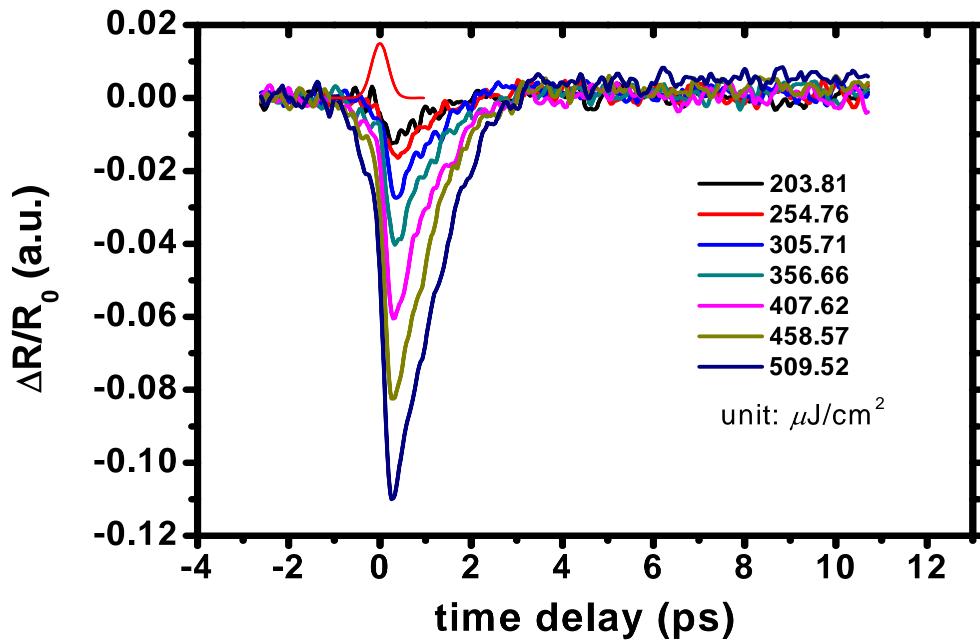

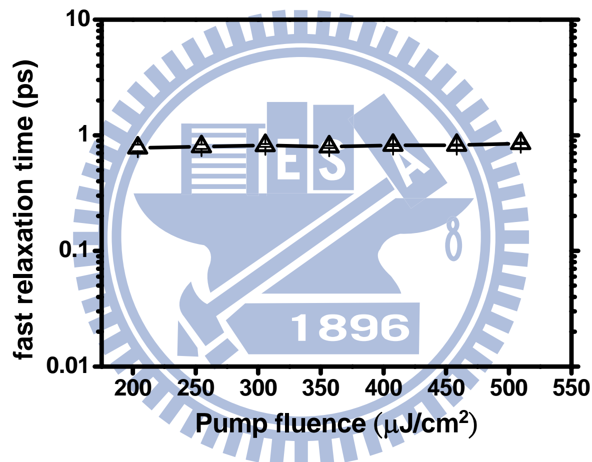

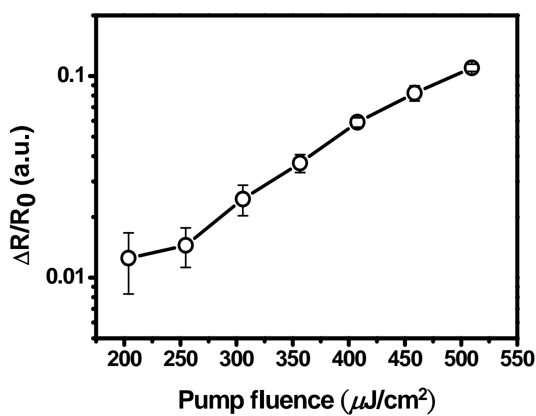

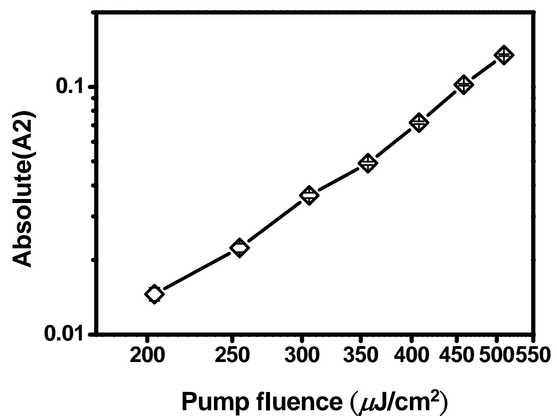

Figure 4-7. The time evolution of transient reflectivity change of InN LT nanorod and the ultrafast carrier dynamic information.

4-3.2 Concentration Dependent Carrier Lifetime

In this work, the carrier dynamics of the free carrier concentration of Mg-doped InN range from 4.33×10^{17} to 3.7×10^{18} cm^{-3} were investigated. The Mg-doped and undoped InN are excited at the pump fluence of 0.356 mJ/cm^2. Our observation nearly shows an inverse relationship between carrier lifetime and free carrier concentration due to the increased electron trapping by the defect. In addition to carrier concentration, defect density in materials significantly influences nonradiative lifetime as well. It may explain the deviation of inverse relationship between different samples.

Reference

[4-1] S. Prabhu and A. Bengulkar, “Dynamics of the pump-probe reflectivity spectra in GaAs and GaN,” J. Appl. Phys. **95** 7803 (2004).

[4-2] T. Korn, ” Femtosekunden-spektroskopie an LT-gaas und Microcavities,” (2000)

[4-3] T. Korn, A. Franke-Wiekhorst, S. Schnull, and I. Wilke, “ Characterization of nanometer As-clustes in low-temperature grown GaAs by transient reflectivity measurements,” J. Appl. Phys. **91**, 2333 (2002)

[4-4] S. Sze, *Physics of Semiconductor Devices* (John Wiley & Sons, 1991)

[4-5] F. Chen, A. Carwright, H. Lu, and W. Schaff, “Ultrafast carrier dynamics in InN epilayers,” J. Crystal Growth **269**, 10 (2004)

[4-6] X.-C. Zahng and D. Auston, “Optoelectronic measurement of semiconductor surfaces and interfaces with femtosecond optics,” J. Appl. Phys. **71** 326 (1992)

[4-7] P. Yu and M. Cardona, *Fundamentals of Semiconductors* (Springer, 2001)

[4-8] M. Nakajima, M. Hangyo, M. Ohta, and H. Miyazaki, “Polarity reversal of terahertz waves radiated from semi-insulating InP surfaces induced by temperature,” Phys. Rev. B **67**,195 308 (2003)

[4-9] O. Madelung, M. Schulz, and H. Weiss, *Landolt-Bornstein: New Series, Group III Vol. 17a* (Springer-Verlag, 1982)

[4-10] F. Bechstedt and J. Furthmuller, “Do we know the fundamental energy gap of InN?” J. Crystal Growth **246**, 315 (2002)

[4-11] B. R. Bennett. R. A. Soref. and J. A. Del Alamo, “Carrier-Induced Change in Refractive Index of InP, GaAs, and InGaAsP,” IEEE J. Quantum Elect. **26**, 113 (1990)

[4-12] I. Mahboob, T. D. Veal, and C. F. McConville, H. Lu, and W. J. Schaff, “Intrinsic Electron Accumulation at Clean InN surfaces,” Phys. Rev. Lett. **92** 036804 (2004)

[4-13] A. Othonos, M. Zervos, and M. Pervolaraki, “Ultrafast Carier Relaxation InN Nanowires Grown by Reactive Vapor Transport,” Nanoscale Res. Lett. **4** 122-129 (2009)

[4-14] E. Lioudakis, A. Othonos, E. Dimakis, and A. Georgakilas, "Femtosecond time-resolved study in InGaN (0001) ultrathin epilayers: Effects of high indium mole fraction and thickness of the films," Appl. Phys. Lett. **89** 241109 (2006)

[4-15] R. Ascazubi, I. Wilke, S. Cho, H. Lu, and W. J. Schaff, "Ultrafast recombination in Si-doped InN," Appl. Phys. Lett. **88** 112111 (2006)

[4-16] H. Ahn, C. H. Chuang, Y. P. Ku, and C. L. Pan, "Free carrier dynamics of InN nanorods investigated by time-resolved terahertz spectroscopy," J. Appl. Phys. **105** 023707 (2009)

[4-17] Y. M. Chang, Y. L. Hong, and S. Gwo, "Direct probe of the built-in electric field o Mg-doped a-plane wurtzite InN surfaces with time-resolved electic-field-induced second harmonic generation," Appl. Phys. Lett. **93** 131106 (2008)

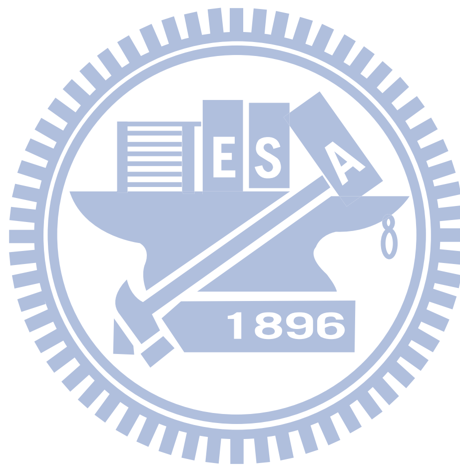

Chap 5. Conclusions and Future Work

5.1 Conclusions

We calculated the second-order optical response of bulk and surface electric field of InN. The calculated results resolve the divergence of larger incident angle of THz due to Fresnel loss and they describes well the azimuthal angle- and polarization-dependence of THz radiation, which is due to the competition between transient current and optical rectification. From azimuthal angle dependence of second harmonic generation, we demonstrated that bulk electro-dipole contribution dominates any surface terms in noncentrosymmetric crystal. The parameters obtained from the best fitting to the azimuthal angle dependent emitted THz radiation are well consistent to the calculated results. We investigated the transient carrier dynamics for InN epilayer and nanorods via time-resolved optical pump-probe technique. The time evolution of transient reflectivity change of InN was found to be the interplay of photoinduced absorption and band filling. The fluence independent lifetime of InN epilayer is regarded as defect-related recombination time.

5.2 Future work

From TREFISH measurement [4-17], Mg-doped a-plane InN film has observed strong built-in electric field in surface. The strong surface electric field may influence THz radiation from InN surface and carrier dynamics in surface region. We will base on analysis in this work to examine optoelectronic properties of Mg-doped InN. Up to now, there is little discussion about photon energy dependent carrier dynamics in InN epilayer and nanorod. Large photon energy variation of probe beam has been used to determine the photoinduced absorption in InN nanowire [4-13] and rich-In InGaN [4-14]. From photon energy dependent carrier dynamics, we can determine that specific dynamics (BGR, PA etc.) in InN epilayer and nanorod.